symmetry

MDPI

Article

Single-Variable Multi-Criteria Optimization of Solid-Phase Volume Fraction in Solid–Liquid Mixing System of High-Viscosity Polyurethane Adhesive Based on CFD Coupled with Machine Learning

Bin He, Xurong Teng, Long Fan and Renlong Liu *

College of Chemistry and Chemical Engineering, Chongqing, University, Chongqing 400044, China; hbgxy2002hb@163.com (B.H.)
* Correspondence: lrl@cqu.edu.cn

Abstract

The solid-phase volume fraction is a core process parameter that determines the mixing quality of high-viscosity polyurethane adhesives. It exhibits complex nonlinear couplings with mixing homogeneity, rheological properties, and energy consumption. Traditional trial-and-error experiments and standalone CFD simulations are hindered by high costs, long computational cycles, and inefficient parameter optimization processes. Consequently, these limitations prevent them from satisfying industrial-scale process optimization demands. To address these challenges, this study proposes a single-variable, multi-criteria intelligent optimization method integrating CFD with machine learning. This study uses a 5000 L industrial stirred reactor as the research object. Twelve typical operating conditions were designed within the 8–32% solid-phase volume fraction range. Numerical simulations were conducted based on the laminar Mixture multiphase flow model. These simulations established a small-sample, high-fidelity operating condition database. To mitigate underfitting caused by limited CFD data, an adaptive cubic spline interpolation algorithm was employed for dataset augmentation. Subsequently, a comparative analysis was conducted between Gaussian process regression (GPR) and support vector regression (SVR) as small-sample surrogate models. Test results demonstrate that the GPR model achieves a coefficient of determination (R^2) of 0.968, with significantly superior prediction accuracy and generalization performance compared to the SVR model. This study uses the solid-phase volume fraction as the sole decision variable. A five-criteria optimization model was constructed based on the optimal GPR surrogate, combined with the NSGA-II algorithm and ideal point decision criterion. Three optimal operating modes were identified—balanced, low-energy, and high-dispersion—tailored for different production scenarios. The proposed integrated collaborative optimization approach effectively reduces process development costs. It also provides comprehensive theoretical foundations and technical references for intelligent control and energy-efficient production of high-viscosity non-Newtonian solid–liquid mixing systems.

Keywords: computational fluid dynamics; machine learning; Gaussian Process Regression; multi-objective optimization; solid–liquid two-phase flow; stirring and mixing; polyurethane adhesive

Check for updates

Academic Editor: Theodore E. Simos

Received: 1 June 2026
Revised: 8 July 2026
Accepted: 17 July 2026
Published: 20 July 2026

Copyright: © 2026 by the authors. Licensee MDPI, Basel, Switzerland. This article is an open access article distributed under the terms and conditions of the Creative Commons Attribution (CC BY) license.

1. Introduction

High-performance polyurethane adhesives are widely used in high-end manufacturing industries such as new energy and aerospace. This is due to their strong structural designability and excellent comprehensive mechanical properties. In industrial production, inorganic fillers like molecular sieves and calcium carbonate are often added to optimize the mechanical properties and usage characteristics of the adhesive [1,2]. The solid-phase volume fraction of the filler is a core parameter in the mixing process. It directly regulates the rheological properties of the adhesive and affects the flow field pattern in the reactor, particle dispersion efficiency, and mixing energy consumption [3]. This parameter exhibits a clear trade-off: too low a solid-phase volume fraction fails to achieve the desired filler modification effect, while too high a content can lead to particle agglomeration and equipment overload [4]. Balbinot [3] demonstrated that silver core–shell particles, used as antibacterial fillers in adhesive resins, can modulate the composite's mechanical properties while maintaining processability. This finding highlights the critical role of filler content in balancing functionality and mixing performance. Therefore, investigating the influence of solid-phase volume fraction on the high-viscosity solid–liquid two-phase mixing system and optimizing process parameters hold significant engineering importance for improving quality and reducing costs in the industrial production of polyurethane adhesives.

Currently, the mainstream research methods for solid–liquid two-phase stirring and mixing problems mainly fall into three categories: empirical trial and error, physical experiments, and CFD numerical simulation [5]. CFD numerical simulation offers high precision, visualization capability, and low cost. It can accurately capture the transient flow field structure, interphase coupling effects, and spatial distribution characteristics of solid-phase volume fraction in stirred tanks. It can also reveal the internal correlation between process parameters and mixing performance from a mechanistic perspective. It has now become an indispensable research tool in the field of multiphase stirring [6]. Relevant existing studies have preliminarily explored the influence laws of solid-phase volume fraction on particle suspension state, local concentration distribution and mixing efficiency by adopting CFD technology [7]. Nevertheless, the single CFD simulation mode still has obvious limitations. Its modeling process is complicated and requires operators to possess high professional competence. High-fidelity transient simulation involves massive computation, and the calculation cycle for a single working condition can last for several days. In addition, the simulation accuracy is highly dependent on boundary conditions and model parameters. This accuracy usually requires verification through costly physical experiments [8,9]. For instance, Shuai [8] conducted numerical simulations of hydrodynamics and mixing characteristics of high-viscosity non-Newtonian fluid in twin-shaft kneaders, revealing the complex flow patterns and dead zones that arise at elevated viscosities. Zheng [9] performed numerical simulations and experimental investigations of gas–liquid two-phase flow in a complex microchannel, showcasing the challenges of multiphase mixing at small scales. These studies collectively highlight that while CFD is powerful, its application to high-viscosity and multiphase systems still faces significant computational and modeling challenges. The above drawbacks greatly restrict the application of pure CFD simulation in engineering design scenarios such as batch screening of multiple working conditions and global parameter optimization.

Recently, data-driven technologies, particularly machine learning, have provided a novel research paradigm for modeling and parameter optimization of complex industrial nonlinear processes [10]. Machine learning models can autonomously learn the nonlinear mapping relationships between input process parameters and output performance metrics based on limited high-fidelity CFD data or experimental data. Once the model training converges, they can rapidly predict performance under new operating conditions with

minimal time cost, enabling fast exploration of the entire parameter space and optimal parameter screening. The deep integration of CFD mechanistic simulation with machine learning has given rise to a collaborative optimization framework: CFD sample generation, machine learning surrogate modeling, and intelligent algorithm global optimization. This paradigm has emerged as a cutting-edge research direction in process engineering [11]. This framework combines the mechanistic nature of CFD models with the efficiency of machine learning models, effectively addressing the limitations of single-method approaches. Several recent studies have further advanced this paradigm. For instance, Trávníková [12] employed physics-informed neural networks (PINNs) to develop a surrogate model for flow field prediction in stirred tanks, significantly reducing data requirements while maintaining prediction accuracy. Maionchi [13] integrated Gaussian Process Regression with Genetic Algorithms to optimize micromixer geometry, demonstrating that this surrogate-assisted approach could efficiently navigate the multi-objective design space with minimal CFD evaluations. These studies collectively confirm that surrogate-model-based optimization is a mature and powerful tool for tackling complex multiphase mixing problems.

Some scholars have applied CFD-ML coupling methods to the field of mixing, with research primarily focusing on impeller structure optimization and single-metric mixing time prediction [14,15]. However, systematic studies addressing high-viscosity non-Newtonian fluid-solid particle two-phase systems remain scarce. Such studies would need to use solid-phase volume fraction as the core decision variable while simultaneously balancing conflicting objectives such as stirring energy consumption, solid-phase dispersion uniformity, shear field intensity, mixing kinetic efficiency, and final mixing quality. Most existing studies only conduct single-objective optimization and fail to fully consider the coupled effects of the unique rheological properties of high-viscosity systems on multi-dimensional mixing metrics [16–19]. As a result, their findings are difficult to directly adapt to the industrial production requirements of polyurethane adhesives.

Compared with previous CFD-ML studies on stirred tanks, solid–liquid mixing, and non-Newtonian systems, this study offers four principal novelties: First, it targets a high-viscosity polyurethane adhesive non-Newtonian solid–liquid system, with the solid-phase volume fraction as the core decision variable, diverging from prior work on Newtonian fluids or gas–liquid systems. Second, it establishes a five-dimensional multi-objective model covering stirring power, solid-phase distribution uniformity, volume-averaged shear rate, mixing time, and final mixing uniformity. This contrasts with single- or bi-objective optimization in previous studies. Third, it employs adaptive cubic spline interpolation for small-sample augmentation with a strict "split-first, augment-later" protocol to prevent data leakage. Fourth, three production-scenario-specific optimal conditions are derived from the Pareto front via ideal-point decision-making, providing directly applicable process parameters for industrial practice.

While real mixing systems involve multiple operational parameters, this study deliberately selects the solid-phase volume fraction as the sole decision variable while holding the impeller speed constant. This scoping is driven by practical engineering priorities: in the industrial production of high-viscosity polyurethane adhesives, the filler solid-phase volume fraction is the most sensitive parameter, directly dictating the formulation's rheological behavior, product functionality, and equipment overload limits. Isolating this primary variable allows us to precisely map its nonlinear impact on the mixing dynamics without confounding effects from secondary operational factors. Consequently, the optimization outcomes yield highly focused, actionable guidance for process engineers. To address potential limitations in generalizability arising from this single-variable approach, the proposed modular CFD-ML architecture is inherently extensible. It provides a robust

foundational framework to incorporate additional design variables, such as impeller speed and geometric configurations, in future comprehensive optimizations.

Based on this, this study takes a 5000 L industrial-grade polyurethane stirred reactor as the research object. With the stirring speed kept constant, it focuses on the multi-objective collaborative optimization of solid-phase volume fraction and conducts comprehensive research including simulation under working conditions in a wide range, data augmentation for small samples, performance comparison of multiple models, and intelligent optimization of high-dimensional multi-objective problems. The overall research framework is as follows. Firstly, high-fidelity CFD simulations are performed under working conditions with solid-phase volume fractions ranging from 8% to 32% in a wide interval. Multi-dimensional mixing performance indicators are systematically collected to establish a dedicated dataset for small samples. Secondly, the adaptive cubic spline interpolation algorithm is adopted to expand the original dataset, so as to break the bottleneck of CFD modeling with small samples. Two machine learning models suitable for small samples, namely GPR and SVR, are compared to select the optimal surrogate model. Finally, a five-dimensional multi-objective optimization mathematical model is built based on the optimal surrogate model. The NSGA-II algorithm is used to obtain the Pareto optimal solution set, and typical recommended working conditions are selected according to the differentiated production requirements in industry. The research findings can provide direct guidance for the optimization of stirring processes of polyurethane adhesives, and also offer a reusable standardized research scheme for the intelligent parameter regulation of high-viscosity multiphase stirring processes.

2. Models and Methods

This study uses a 5000 L industrial-scale stirred reactor as the research platform. It investigates the influence of solid-phase volume fraction on the mixing performance of high-viscosity solid–liquid two-phase systems and identifies optimal parameter solutions. The overall research process includes the following steps: (1) determining the simulation range of solid-phase volume fraction and selecting typical operating conditions; (2) collecting multi-dimensional performance indicators through CFD numerical simulation (Workbench 2021) to construct an initial small-sample dataset; (3) expanding the sample size using an adaptive cubic spline interpolation algorithm; (4) training two types of machine learning models (GPR and SVR; MATLAB R2025a) and selecting the optimal surrogate model based on three evaluation metrics; and (5) establishing a five-objective optimization model with solid-phase volume fraction as the decision variable, solving the Pareto front using the NSGA-II algorithm, and identifying the optimal operating conditions suited for different production scenarios. The overall research framework is illustrated in Figure 1.

2.1. CFD Numerical Simulation

This study focuses on a low-speed, high-viscosity solid–liquid two-phase mixing system, where the fluid in the reactor primarily exhibits laminar flow with no significant turbulent pulsation effects. Therefore, the Mixture multiphase flow model coupled with a laminar flow solver was selected for simulation. The liquid phase medium is castor oil, and the solid-phase medium is a composite filler of molecular sieves and calcium carbonate. The coupling behavior between the two phases is characterized by mixed density, mixed viscosity, and interphase slip velocity, eliminating the need for additional turbulent stress terms, thereby improving computational convergence and efficiency while ensuring the fidelity of physical mechanisms. The study employs three fundamental equations: the continuity equation, momentum conservation equation, and species transport equation. These equations comprehensively describe the motion and mixing process of the two-phase

fluid. Additionally, the spatial distribution of the solid-phase volume fraction is tracked in real-time via the species transport equation, providing data support for quantitative calculations of metrics such as mixing uniformity [20]. The expressions for each governing equation are as follows:

Continuity equation:

$$\frac{\partial \rho_m}{\partial t} + \nabla \cdot \left(\rho_m \overrightarrow{v_m}\right) = 0 \quad (1)$$

where ρ_m is the mixture density (kg/m^3); $\overrightarrow{v_m}$ is the average velocity of the mixed phase (m/s), t is time (s). The mixture density is calculated by the mass-weighted average method:

$$\rho_m = \alpha_l \rho_l + \alpha_s \rho_s \quad (2)$$

In the equation, α_l and α_s represent the volume fractions of the liquid and solid phases, respectively, satisfying $\alpha_l + \alpha_s = 1$; ρ_l and ρ_s denote the densities (kg/m^3) of the liquid and solid phases. The density of the composite mixed powder can be calculated using the mass-weighted average method.

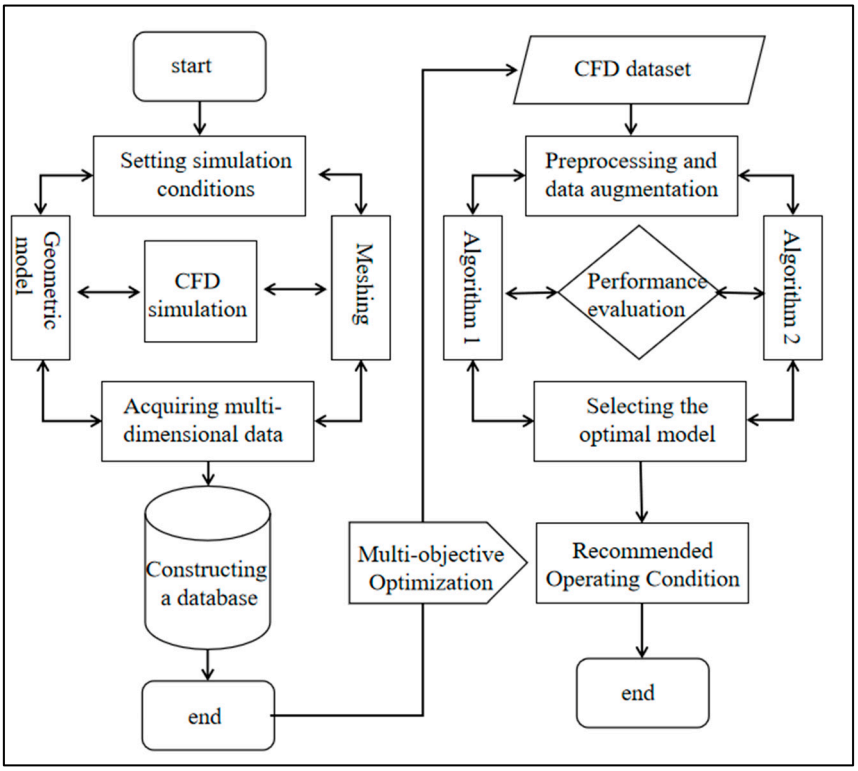


Figure 1. The overall research framework of this work.

Momentum conservation equation:

$$\frac{\partial\left(\rho_m \overrightarrow{v_m}\right)}{\partial t} + \nabla\cdot\left(\rho_m \overrightarrow{v_m}\overrightarrow{v_m}\right) = -\nabla \cdot p + \nabla \cdot \left(\mu_m\left(\nabla \overrightarrow{v_m} + (\nabla \overrightarrow{v_m})^T\right)\right) + \rho_m \overrightarrow{g} + F \quad (3)$$

where p is the static pressure (Pa); μ_m is the mixture viscosity (Pa·s); $\overrightarrow{g}$ is the gravitational acceleration (m/s^2); and F is the interphase drag force term. Constrained by laminar flow characteristics, the turbulence stress term is neglected in this model. The mixture viscosity is also calculated using the volume-weighted averaging method:

$$\mu_m = \alpha_l \mu_l + \alpha_s \mu_s \quad (4)$$

Transport equation: to track the spatial distribution of solid particles in real time and quantify the mixing process, the transport equation for the solid-phase volume fraction is introduced:

$$\frac{\partial(\alpha_s \rho_m)}{\partial t} + \nabla \cdot (\alpha_s \rho_m \overrightarrow{v_m}) = \nabla \cdot (\Gamma_\alpha \nabla \alpha_s) + S_\alpha \quad (5)$$

In the equation, the Γ_α represents the diffusion coefficient; S_α denotes the source term. Since there are no chemical reactions or phase changes in this study system, $S_\alpha = 0$.

2.1.1. Geometric Modeling and Meshing

(1) Geometric modeling

A geometric model was constructed based on a 5000 L industrial-scale stirred reactor as the prototype. To balance computational efficiency and simulation accuracy, the equipment was rationally simplified. Non-core auxiliary structures such as the jacket, temperature-measuring sleeve, and feed inlet were removed. Only core fluid domain structures like the vessel body, agitator shaft, and multiple sets of impellers were retained. The castor oil colloid under constant temperature conditions was simplified into a homogeneous single-phase liquid medium to reduce simulation redundancy. The total height of the reactor is 2680 mm, featuring three functionally complementary stirring structures: a propeller type, an anchor type, and a high-speed dispersing type, with detailed structural parameters listed in Table 1. This study employed the multiple reference frame method to partition the fluid domain, dividing the entire region into a static vessel domain and multiple dynamic impeller rotation domains, balancing the motion characteristics of rotating components with the boundary adaptability of the static domain. The geometric model and labeled regions are shown in Figure 2.

Table 1. Structural parameters of the agitator.

Symbols		Values (mm)
Inner diameter of the reactor		1900
Height of the reactor		2680
Propeller stirring section		
	Shaft diameter	95
	Rotary axis length	2210
Four-bladed propellers (three sets)	Blade diameter	450
	Rotation zone diameter	480
	Rotation zone height	70
Anchor stirring section		
	Shaft diameter	120
	Rotary axis length	2635
	Blade diameter	1800
	Rotating area width	100
High-speed dispersion section		
	Shaft diameter	120
	Rotating shaft length	2210
Scattering disk (two sets)	Blade diameter	450
	Rotation zone diameter	480
	Rotation zone height	120

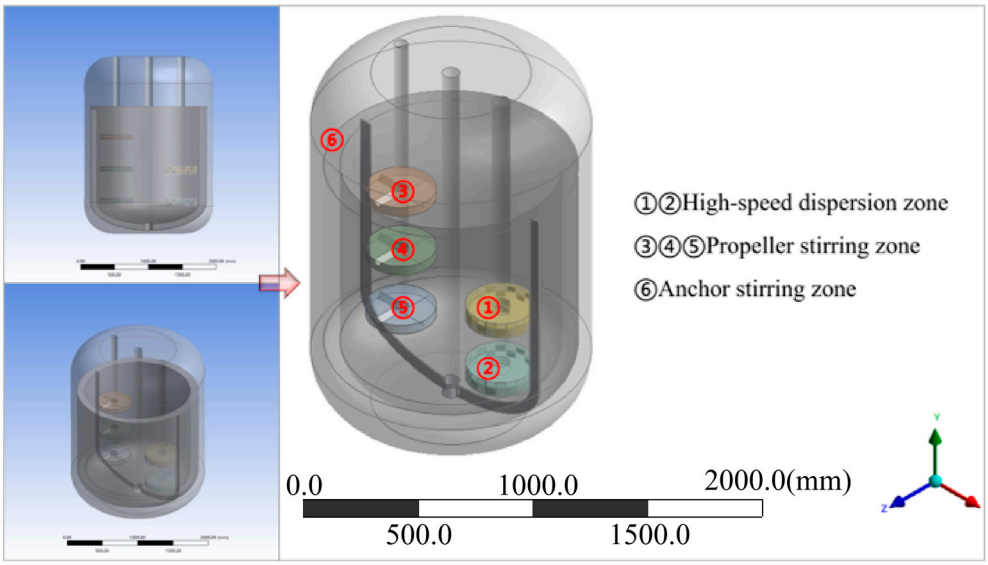


Figure 2. Geometric model of the reactor.

(2) Mesh generation

The quality of mesh generation directly determines the accuracy and reliability of CFD simulation results. Considering the complex flow field structure and large velocity gradients around the impeller, this study employs tetrahedral unstructured meshes to partition the entire domain. This mesh type can flexibly adapt to complex curved surfaces and accurately capture high-gradient flow regions such as vortices and shear layers. During the meshing process, curvature control and proximity layer refinement were enabled to locally refine key areas like the impeller blade surfaces and near-wall regions of the reactor. This approach ensures resolution accuracy in the core flow field while controlling the total number of grid elements, balancing computational accuracy and efficiency. This study employs a grid division scheme primarily based on unstructured grids, with a total of 5,738,685 elements, a minimum orthogonal quality of 0.2, and a maximum aspect ratio of 20.78. The local grid refinement strategy is based on a global base dimension of 189.75 mm and a growth factor of 1.2. It utilizes curvature capture, proximity capture, and feature elimination functions to perform static automatic refinement of geometric features. Mesh integrity tests show that the minimum cell volume is 1.545097×10^{-10}, with no negative volume elements in the entire domain, meeting the requirements for simulation. The reactor mesh distribution is illustrated in Figure 3.

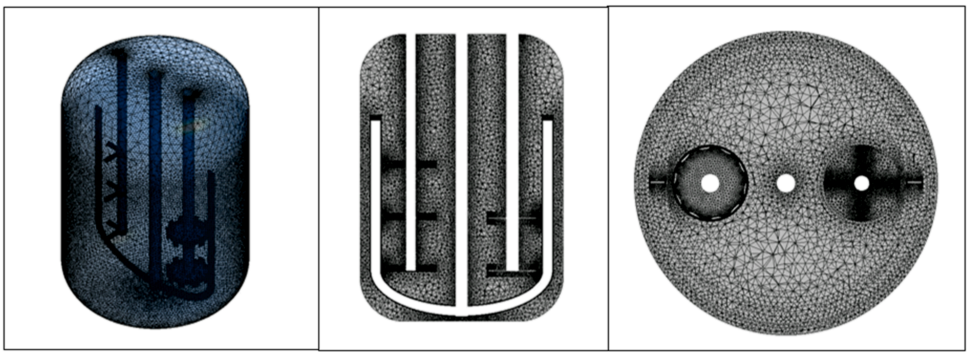


Figure 3. Reactor Grid Diagram.

(3) Mesh independence

To evaluate the impact of grid density on simulation results, this study conducted a grid independence analysis. We selected the radial velocity at line 1 as a convergence metric and compared results across three grid sizes (57386850; 6809638; 7303568), as shown in Figure 4.

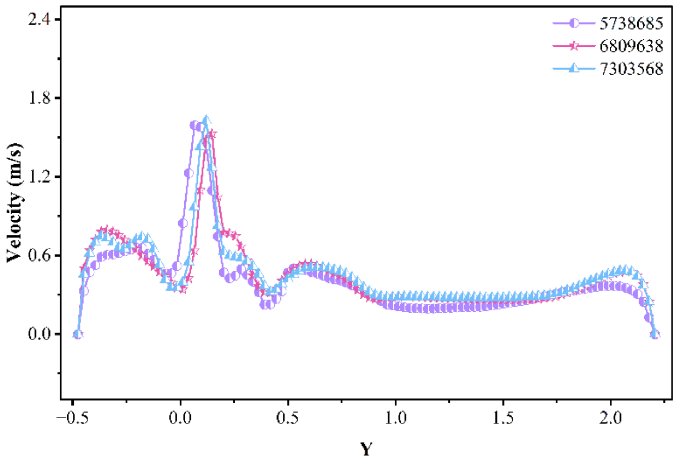


Figure 4. Mesh Independence Verification Results.

It can be observed that in the stable region where Y > 0.5, the radial velocity distribution curves at the three grid densities nearly coincide entirely. This indicates no significant change in the overall trend of radial velocity after grid refinement. It also demonstrates that the grid density adequately captures the macroscopic characteristics of the flow field. In the region of significant variation (near the stirrer, where Y = 0–0.5), minor differences exist among the curves, but their peak locations and fluctuation patterns remain consistent, suggesting that local details in this critical region have converged. Therefore, considering computational time and resource requirements, a grid density of 5,738,685 elements was selected as the final choice.

2.1.2. Boundary Conditions and Solution Settings

The parameter settings for the castor oil liquid-phase medium under ambient temperature conditions are as follows: density 955 kg/m^3, dynamic viscosity 0.95 Pa·s [21]. The transient calculation mode is selected for the solution, and the rotation direction and speed sign of the stirring shaft are determined according to the right-hand rule. Rotating components such as blades and the stirring shaft uniformly adopt absolute velocity boundary conditions. The inner wall of the vessel is set as a no-slip boundary to adapt to the wall flow characteristics of high-viscosity fluid mixing. The residual convergence threshold for the simulation is set to 10^{-5}, with a single time step of 0.01 s. To quantitatively characterize the flow regime of the system, this study calculated the stirring Reynolds numbers for each agitator blade. The fluid density was 955 kg/m^3, and the dynamic viscosity was 0.95 Pa·s. The rotational speeds and corresponding Reynolds numbers for each blade were as follows: three sets of helical blades at 100 rpm (D = 0.45 m), Re ≈ 339; anchor-type blades at 20 rpm (D = 1.8 m), Re ≈ 1085; two sets of high-speed dispersion disks at 340 rpm (D = 0.45 m), Re ≈ 1153. All these Reynolds numbers are significantly below the laminar-turbulent transition threshold (typically Re < 10^4), and with the overall system viscosity reaching 0.95 Pa·s, turbulent pulsation is substantially suppressed. Therefore, it is reasonable to consider the entire system to exhibit a predominantly laminar flow regime. Thus, a laminar solver was employed for the simulation, which is appropriate for the predominantly laminar flow regime in this high-viscosity system. In addition, the rotational speeds of all stirring

paddles in this study were set as follows: the three sets of propeller paddles operated at 100 rpm, the anchor paddle at 20 rpm, and the two sets of high-speed dispersion disks at 340 rpm. These speeds remained constant throughout the study to ensure comparability when using solid-phase volume fraction as the sole decision variable.

Based on the functional properties of fillers and industrial production limits, the core research range for solid-phase volume fraction is defined as 10–30%. Here, 10% represents the minimum critical addition level for functional fillers to achieve water absorption, defoaming, and reinforcement effects. Meanwhile, 30% is the empirical upper limit for stable mixing of high-viscosity non-Newtonian colloids in industrial settings. Beyond this limit, issues such as viscosity spikes, equipment overload, and mixing failure may occur [22]. To broaden the model's applicability, define process safety boundaries, and enhance extrapolation robustness, this study extends the simulation range bidirectionally by adding an 8% low-concentration control group and a 32% over-limit exploratory group.

The working condition sampling adopts a stratified strategy of "boundary anchoring and core densification": anchoring the upper and lower boundary conditions within the 8~32% global range, while conducting high-density sampling in the 20~25% optimal solution estimation core interval to precisely capture peak mixing performance and parameter mutation characteristics. Ultimately, 12 representative working conditions were selected for CFD simulations, with the specific sampling scheme detailed in Table 2.

Table 2. Twelve Typical Simulation Conditions.

Serial Number	Solid-Phase Volume Fraction (%)	Serial Number	Solid-Phase Volume Fraction (%)
1	8.0	7	22.0
2	10.0	8	23.0
3	12.0	9	25.0
4	15.0	10	28.0
5	18.0	11	30.0
6	20.0	12	32.0

2.1.3. Justification of the Newtonian Fluid Assumption

In this study, the liquid phase was modeled as a Newtonian fluid with constant viscosity (castor oil, density 955 kg/m^3, dynamic viscosity 0.95 Pa·s). Although industrial polyurethane adhesives containing solid fillers typically exhibit shear-thinning or yield-stress behavior, this simplification is justified by the following considerations.

First, the primary objective of this study is to establish and validate a CFD-ML optimization framework for solid–liquid mixing systems, rather than to precisely replicate the absolute numerical values of a specific adhesive formulation. The Newtonian assumption preserves the essential physics of fluid mixing, including convective transport, shear-induced dispersion, and solid–liquid interaction. It also substantially reduces computational complexity. This simplification strategy has been widely adopted in similar CFD-ML coupling studies focused on methodology development. Second, from an engineering design perspective, the Newtonian assumption underestimates the apparent viscosity increase at elevated solid-phase volume fractions, particularly in the upper range of the investigated interval (25–32%). Consequently, the predicted power consumption and mixing time in this study represent conservative lower-bound estimates relative to actual non-Newtonian systems. The optimal solid-phase volume fraction ranges identified based on this assumption therefore provide a safety margin for practical engineering process design. Third, castor oil was selected as the surrogate liquid phase because its room-temperature viscosity (0.95 Pa·s) falls within the typical viscosity range of industrial polyurethane prepolymers.

Regarding the solid-phase physical properties, the solid phase is a composite filler of molecular sieves and calcium carbonate at a mass ratio of 3:1 (accounting for 5.60% and 61.19% of the total formulation, respectively), with a weighted-average density of 2100 kg/m^3, a mean particle size of 15 μm (range 5–30 μm), and irregular angular morphology. The interphase interactions are characterized through the Mixture multiphase model coupled with a laminar flow solver. In this model, mixture density and mixture viscosity are computed via volume-weighted averaging. No separate interphase drag model is required. This treatment is appropriate for high-viscosity solid–liquid systems under laminar flow conditions.

Nevertheless, we acknowledge that non-Newtonian effects may become increasingly significant at solid-phase volume fractions exceeding 25%. Future work will incorporate Carreau-Yasuda or Herschel–Bulkley constitutive models calibrated against experimental rheological data. This will quantify the influence of shear-thinning and yield stress on mixing performance. It will also further enhance the predictive accuracy and industrial applicability of the proposed framework.

2.1.4. Model Validation

The model validation in this study was conducted using a stirrer with dimensions nearly identical to those employed in the reference literature (Zalc et al. [23]). Zalc et al. [23] performed laser-induced fluorescence measurements under laminar flow conditions in a reactor equipped with three Rushton turbine blades, providing a well-established benchmark case for flow simulation in laminar stirred tanks. We first simulated the flow field within this reactor at a Reynolds number (Re) of 20, then compared the simulated radial velocity distribution with the experimental data presented by Zalc et al. [23]. As shown in Figure 5, the predicted curve lies centrally along the radial direction of the tank, extends vertically across its entire height, and aligns precisely with the blade configuration. The CFD predictions (red scattered points) exhibit minimal deviation from the experimental values (black solid line) throughout the vertical range (0.00–0.35 m), falling within acceptable limits; both datasets demonstrate identical multi-peak waveform characteristics that accurately capture the velocity distribution induced by multi-stage blades. To quantify consistency, the following statistical parameters were calculated: Pearson correlation coefficient r = 0.9684 ($p < 0.0001$), Spearman's rank correlation coefficient ρ = 0.9289 ($p < 0.0001$), root mean square error (RMSE) = 0.0175, mean absolute error (MAE) = 0.0130, and mean square error (MSE) = 0.000307. Both Pearson and Spearman coefficients approach 1, indicating a strong linear and monotonic correlation between CFD predictions and experimental data. Lower RMSE and MAE values further confirm minimal absolute deviations within acceptable limits for engineering applications. These results demonstrate that the laminar mixture multiphase flow model employed in this study accurately reproduces the reference flow field with high fidelity.

2.2. Framework Construction for Machine Learning Methods

2.2.1. Selection of CFD Evaluation Indicators

High-precision surrogate models rely on quantitative indicators that possess clear physical significance, high parameter sensitivity, and industrial relevance. This paper selects six indicators: solid-phase volume fraction, volume-averaged shear rate, stirring power, solid-phase distribution uniformity, mixing time, and final mixing uniformity, covering five dimensions: material properties, energy consumption level, shear environment, mixing efficiency, and mixing quality. The definitions and calculation formulas of each indicator are as follows:

(1) Solid-phase volume fraction: The sole decision variable, representing the overall loading level of solid fillers in the stirred tank, which directly determines the rheological properties and fundamental flow state of the system. It is calculated using the reactor's effective volume-weighted average:

$$\alpha_s = \frac{1}{V}\int_V \varnothing_s dV \tag{6}$$

where α_s represents the volume-averaged solid-phase volume fraction; V stands for the effective fluid volume of the reactor (m^3); $\varnothing_s$ denotes the local instantaneous solid-phase volume fraction.

(2) Volume-averaged shear rate: Quantifies the overall intensity of the shear force field within the reactor, directly affecting the agglomeration and fragmentation of solid particles as well as interphase mass transfer efficiency. It is a key parameter for regulating the modification effect of colloids.

$$\dot{\gamma_{avg}} = \frac{1}{V}\int_V \dot{\gamma} dV, \dot{\gamma} = \sqrt{2S:S}, S = \frac{1}{2}(\nabla u + (\nabla u)^T) \tag{7}$$

where $\dot{\gamma_{avg}}$ denotes the volume-averaged shear rate (s^{-1}); S represents the strain rate tensor; u stands for the instantaneous velocity vector of the fluid (m/s). A high shear rate can break up particle agglomerates, yet it will simultaneously increase the stirring energy consumption.

(3) Stirring Power: An indicator for evaluating the economy of production energy consumption, converted from the rotational torque of the impeller:

$$P = M \cdot \frac{2\pi N}{60} \tag{8}$$

where P represents the stirring power (W); M is the stirring paddle torque ($N \cdot m$); and N denotes the stirring speed (r/min). The power is calculated by integrating the torque on the blade surface.

(4) Uniformity of solid-phase distribution: This evaluates the degree of dispersion uniformity of solid particles within the reactor space under steady-state conditions, reflecting the static mixing quality of agitation. It is calculated using the standard deviation method of monitoring point concentrations.

$$\sigma_s = \sqrt{\frac{1}{M}\sum_{i=1}^{M}(\phi_{s,i} - \alpha_s)^2}, U_s = 1 - \frac{\sigma_s}{\alpha_s} \tag{9}$$

where the uppercase U_s with a subscript s represents the uniformity index of the solid-phase distribution. A value closer to 1 indicates better particle dispersion. M is the number of monitoring points inside the reactor; $\phi_{s,i}$ denotes the local solid-phase volume fraction at the i-th monitoring point.

(5) Mixing time: This is an indicator for evaluating dynamic mixing efficiency. It refers to the shortest time required after tracer introduction for the concentration at all monitoring points to stabilize within ±5% of the final average concentration (95% mixing standard).

$$t_m = min\{t | \frac{c_i(t) - c_\infty}{c_\infty} \leq 0.05, \forall i\} \tag{10}$$

where t_m denotes the mixing time (s); $c_i(t)$ represents the tracer concentration at the ith monitoring point at time t; c_∞ is the final uniform concentration after complete mixing. A shorter mixing time indicates higher mixing kinetic efficiency.

(6) Final mixing uniformity: It characterizes the overall mixing quality of the system after reaching complete steady state, calculated using the normalized vari-

ance decay method to eliminate interference from absolute concentration levels on evaluation results.

$$G = 1 - \frac{\sigma^2}{\sigma_0^2} \tag{11}$$

where G represents the final mixing uniformity. The closer the value is to 1, the more uniform the mixing. Sigma squared refers to the variance of tracer concentrations at each monitoring point after the system reaches a steady state. σ_0^2 denotes the variance of tracer concentrations at the initial moment (t = 0) after the tracer is added.

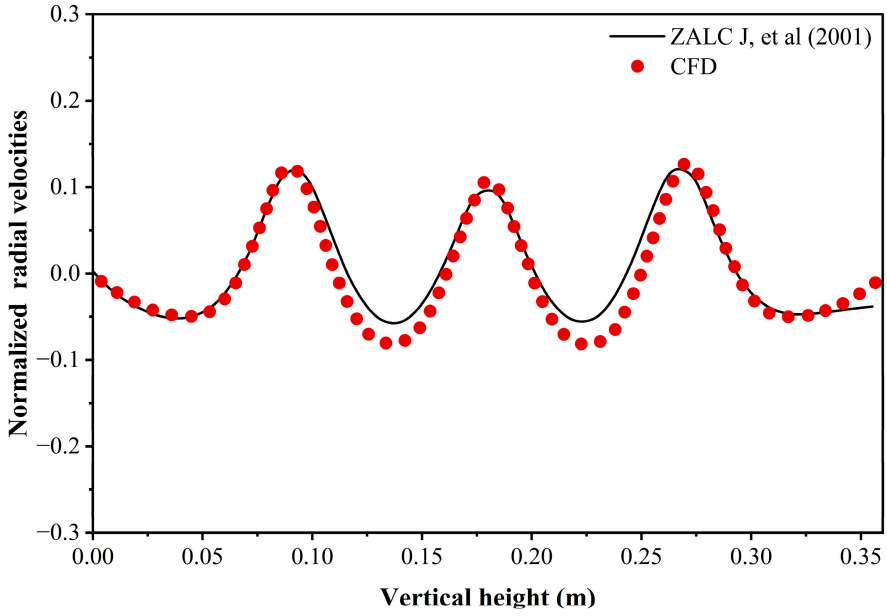


Figure 5. Comparison of model validation results. The validation data for the laminar model in the figure are from reference [23].

2.2.2. Dataset Construction and Enhancement

To completely avoid data leakage, this study adopts a standardized "split-first, augment-later" workflow. The 12 original samples were randomly divided into 8 training base sets and 4 independent test sets. Data augmentation via adaptive cubic spline interpolation was performed only on the training base sets. The newly generated virtual samples were combined with the original training samples to form an augmented training set. The independent test sets remained isolated throughout the entire process, never participating in interpolation, training, or optimization, and were solely used for final model generalization performance validation.

The selection logic for the data augmentation solution operates on two levels: First, cubic spline interpolation is chosen as the base algorithm. The process-performance parameter variations in CFD simulation data exhibit continuity and smoothness characteristics, and cubic spline interpolation can generate fitted curves with continuous first and second derivatives. This avoids the abrupt turning points of linear interpolation and the non-physical oscillations of high-order polynomial interpolation, ensuring that the newly added virtual samples adhere to fluid mixing physics. To justify the applicability of interpolation in this high-viscosity non-Newtonian system without introducing unphysical artifacts, we draw upon evidence from similar systems. According to Shuai et al. [8], macroscopic mixing metrics in high-viscosity non-Newtonian systems follow smooth trajectories rather than discontinuous phase transitions, provided the system avoids flow deadlock. Within the 8–32% solid-phase volume fraction range, continuous filler addition induces gradual rheological variations without sudden singularities. Tamburini [6] demonstrated that solid-phase

distribution exhibits smooth, continuous gradients with respect to solid-phase volume fraction. This continuity is further supported by similar high-solid systems: Mao [24] confirmed that mixing power and slurry uniformity follow smooth response surfaces with solid-phase volume fraction. Gu [25] verified that mixing time and concentration standard deviation exhibit continuous gradients. These documented continuous behaviors confirm that expanding samples via cubic spline interpolation is physically valid, as its continuous derivatives align with the system's smooth parametric responses.

Second, an adaptive optimization mechanism is introduced. This allows the algorithm to dynamically allocate interpolation points based on the spacing of original samples. It increases sampling density in sparse regions and reduces it in dense regions. This balances sample diversity and redundancy while mitigating overfitting risks.

Cubic spline interpolation method:

The cubic spline interpolation is a piecewise smooth interpolation algorithm. For given sample points (x_0, y_0), (x_1, y_1), …, (x_n, y_n), it constructs cubic polynomials within each subinterval $[x_i, x_{i+1}]$, ensuring the continuity of first and second derivatives at the nodes. The expression for the piecewise interpolation function is as follows [26]:

$$S_i(x) = a_i(x - x_i)^3 + b_i(x - x_i)^2 + c_i(x - x_i) + d_i \tag{12}$$

where a_i, b_i, c_i, and d_i are the undetermined coefficients of the piecewise polynomial. By solving the system of three-moment equations simultaneously and incorporating the boundary constraints, the complete global interpolation function can be obtained.

$$S''_i(x) = \frac{M_{i+1}(x - x_i)}{h_i} - \frac{M_i(x - x_{i+1})}{h_i} \tag{13}$$

where M_i represents the second derivative value at node x_i; h_i represents the length of the subinterval $[x_i, x_{i+1}]$. By performing double integration and applying boundary conditions, the complete interpolation expression can be obtained.

Adaptive interpolation takes sample spacing as the core basis and dynamically adjusts the interpolation density across intervals. While preserving the smoothness of cubic spline interpolation, it automatically allocates varying numbers of interpolation points based on the distance between adjacent data points. This increases sampling density in sparse data regions while reducing redundant computations in dense data areas.

Given n + 1 data points (x_0, y_0), (x_1, y_1), …, (x_n, y_n), where $x_0 < x_1 < \ldots < x_n$, calculate the spacing of each subinterval:

$$h_i = x_{i+1} - x_i \tag{14}$$

Determine the minimum spacing $h_{min} = min\{h_i\}$ and the maximum spacing $h_{max} = max\{h_i\}$.

On the i-th subinterval $[x_i, x_{i+1}]$, the number of interpolation points N_i is determined by the following formula:

$$N_i = N_{min} + \left\lfloor (N_{max} - N_{min}) \cdot \frac{h_i - h_{min}}{h_{max} - h_{min}} + 0.5 \right\rfloor \tag{15}$$

2.2.3. Machine Learning Model Selection

In the context of modeling scenarios with small samples and strong nonlinearity, this paper selects two types of adaptive kernel function algorithms, GPR and SVR, to conduct modeling experiments. These two algorithms do not require massive sample support and can map high-dimensional feature spaces through kernel tricks, accurately analyzing the nonlinear relationship between process parameters and performance indicators [27]. Deep learning models are not considered as alternatives due to their tendency to overfit

with small samples, while linear regression models are excluded for their insufficient fitting capability.

(1) Gaussian Process Regression Model

Gaussian process regression is a nonparametric probabilistic regression model based on the Bayesian framework. It treats the mapping function to be fitted as an infinite-dimensional random Gaussian process. The joint distribution of function values corresponding to any finite sample follows a multivariate Gaussian distribution [28]. This model not only outputs predicted values but also quantifies the confidence interval for each prediction point, facilitating the assessment of prediction uncertainty and meeting the risk management requirements of industrial optimization.

The GPR model is defined by a mean function $m(x)$ and a covariance function (kernel function) $k(x, x')$:

$$f(x) \sim GP\left(m(x), k\left(x, x'\right)\right) \tag{16}$$

This study sets the mean function to zero by default for computational simplicity, and selects the radial basis function and Matern kernel, which are suitable for fluid data, as the covariance kernel functions. For the noisy training dataset:

$$D_I = \{(x_i, y_i) | i = 1,\ 2 \ldots n\} \tag{17}$$

$$y_i = f(x_i) + \epsilon, \epsilon \sim N(0, \sigma_n^2) \tag{18}$$

The key to GPR lies in computing the function value f_* corresponding to the new input point x_*. The posterior predictive distribution remains a Gaussian distribution:

$$p(f_* \mid X,\ y, x_*) = N\left(\overline{f_*}, \vee[f_*]\right) \tag{19}$$

The predicted mean $\overline{f_*}$ bar and the predicted variance or $\vee[f_*]$ are calculated as follows [29]:

$$\overline{f_*} = k_*^T (K + \sigma_n^2 I)^{-1} y \tag{20}$$

$$\vee[f_*] = k(x_*, x_*) - k_*^T (K + \sigma_n^2 I)^{-1} k_* \tag{21}$$

Among them, K is the covariance matrix of the training samples; k_* represents the covariance vector between the training samples and the new sample; the predicted mean is the optimal estimate, and the variance is used to characterize the prediction uncertainty.

(2) Support Vector Regression Model

The support vector regression model is constructed based on the principle of structural risk minimization [30]. Its core objective is to solve for the optimal regression hyperplane. This ensures that the prediction errors of all training samples fall within a predefined tolerance interval ϵ. It also minimizes the complexity of the hyperplane to enhance the model's generalization capability. By employing kernel functions, the original low-dimensional data is mapped to a high-dimensional feature space, enabling nonlinear regression solutions. The original optimization objective function of SVR is as follows:

$$\begin{aligned} &min_{\mathrm{w,b},\xi_\mathrm{i},\xi_\mathrm{i}^*} \frac{1}{2}\|\omega\|^2 + \mathrm{C}\sum_{\mathrm{i}=1}^{\mathrm{n}}(\xi_\mathrm{i} + \xi_\mathrm{i}^*) \\ &\text{s.t.} \quad y_i - [w, \phi(\mathrm{x_i})] - b \le \epsilon + \xi_\mathrm{i} \\ &[w, \phi(x_i)] + b - y_i \le \epsilon + \xi_\mathrm{i}^* \\ &\xi_\mathrm{i}, \xi_\mathrm{i}^* \ge 0, \quad \mathrm{i} = 1, \ldots, n \end{aligned} \tag{22}$$

Among them, w and b are the weight vector and bias term of the hyperplane, respectively; $\phi(\cdot)$ is the high-dimensional space mapping function; C is the penalty coefficient; ξ_i, ξ_i^* are the relaxation variables.

After introducing the Lagrange multiplier to solve the dual problem, the final prediction function can be simplified as:

$$f(x) = \sum_{i=1}^{n} (\alpha_i + \alpha_i^*) k(x_i, x) + b \tag{23}$$

2.2.4. Model Evaluation

Its core objective is to solve for the optimal regression hyperplane. This ensures that the prediction errors of all training samples fall within a predefined tolerance interval ϵ. It also minimizes the complexity of the hyperplane to enhance the model's generalization capability.

(1) RMSE is used to characterize the degree of dispersion between predicted values and actual values. The smaller the value, the higher the model's accuracy.

$$RMSE = \sqrt{\frac{1}{n}\sum_{i=1}^{n}(y_i - \check{y}_i)^2} \tag{24}$$

(2) MAE intuitively reflects the absolute magnitude of prediction errors and is not affected by extreme outliers.

$$MAE = \frac{1}{n}\sum_{i=1}^{n}|y_i - \check{y}_i| \tag{25}$$

(3) R^2 represents the model's ability to explain the variation characteristics of the original data, with a range of [0, 1]. The closer the value is to 1, the better the fit.

$$R^2 = 1 - \frac{\sum_{i-1}^{n}(y_i - \check{y}_i)^2}{\sum_{i-1}^{n}(y_i - \overline{y})^2} \tag{26}$$

where y_i represents the true value from CFD simulation; $\check{y}_i$ denotes the model predicted value; $\overline{y}$ is the average of the true values; n is the number of samples in the test set.

2.2.5. Multi-Objective Optimization of the Optimal Model

Considering the practical production constraints of polyurethane adhesives, this study takes the solid-phase volume fraction x as the sole one-dimensional decision variable, with its feasible range consistent with the simulation interval, i.e., $x \in [0.08, 0.32]$. Five core indicators were selected to construct a multi-objective optimization model: mixing power, solid-phase distribution uniformity, volume-average shear rate, mixing time, and final mixing homogeneity. These five indicators exhibit significant conflicting characteristics: reducing solid-phase volume fraction can decrease mixing energy consumption but worsens solid-phase dispersion; increasing solid-phase volume fraction improves particle uniformity yet raises power consumption and reduces overall mixing quality, making it impossible to simultaneously optimize all indicators through a single parameter.

To adapt to the minimization optimization mechanism of the NSGA-II algorithm and unify the optimization direction, the maximization objectives (solid-phase distribution uniformity and final mixing uniformity) were inversely processed, constructing a standardized five-objective minimization mathematical model:

$$\begin{gathered} minF(x) = [f_1(x), f_2(x), f_3(x), f_4(x), f_5(x)]^T \\ s.t.\ x_{min} \le x \le x_{max} \end{gathered} \tag{27}$$

where $f_1(x)$ represents the stirring power; $f_2(x)$ denotes the uniformity of solid-phase distribution; $f_3(x)$ indicates the volume average shear rate; $f_4(x)$ stands for the mixing time; and $f_5(x)$ represents the final mixing uniformity after reverse transformation.

This study employs the Non-dominated Sorting Genetic Algorithm II (NSGA-II) with an elite strategy to solve the Pareto optimal solution set. The algorithm does not rely on the gradient of the objective function and achieves global optimization through three evolutionary operations: selection, crossover, and mutation, making it suitable for high-dimensional conflicting objective optimization scenarios [31]. The algorithm uses fast non-dominated sorting to classify population levels and introduces crowding distance to maintain the diversity of samples distributed along the Pareto front. During the offspring generation phase, the Simulated Binary Crossover (SBX) and Polynomial Mutation (PM) strategies are adopted to balance the population's global exploration and local exploitation capabilities. Based on pre-experimental results of working conditions, the algorithm's hyperparameters are set as follows: population size N = 100, maximum evolution generations G = 200, crossover probability pc = 0.9, and mutation probability pm = 0.1. During the optimization process, the trained Gaussian Process Regression (GPR) surrogate model is directly called to evaluate objective values, thereby avoiding the high computational costs associated with tens of thousands of CFD simulations.

After iterative solving with the NSGA-II algorithm, a set of Pareto optimal solutions that cannot be simultaneously improved across the five objectives was obtained, denoted as $X^* = \{x_1^*, x_2^*, ..., x_M^*\}$. To select the final recommended operating condition from the M non-dominated solutions for engineering practice, this chapter employs the normalized Euclidean distance method based on the ideal point for posterior decision-making [32].

Firstly, the ideal point (optimal value) of the Pareto solution set for each objective is extracted:

$$f_m^{ideal} = min_{k=1,...,M} f_m(x_k^*) \tag{28}$$

Subsequently, all solutions on the Pareto front undergo linear normalization to eliminate differences in units and magnitudes between objectives:

$$\overline{f_m}(x_k^*) = \frac{f_m(x_k^*) - f_m^{ideal}}{f_m^{max} - f_m^{min}} \tag{29}$$

In the equation, f_m^{max} and f_m^{min} represent the maximum and minimum values of the current Pareto solution set on the m-th objective, respectively. After normalization, the Euclidean distance from each Pareto solution to the ideal point is calculated:

$$D_k = \sqrt{\sum_{m=1}^{5} \left[\overline{f_m}(x_k^*)\right]^2} \tag{30}$$

A smaller distance D_k indicates that the solution has a lower overall deviation from the ideal point across all objectives, meaning the balance among the objectives is optimal. Therefore, the solution corresponding to the minimum distance is selected as the "comprehensive balanced" optimal operating condition. Additionally, to meet the needs of different real-world production scenarios, extreme preference conditions corresponding to single-objective extremes are simultaneously extracted. These scenarios include energy-saving and consumption-reduction orientation or high-efficiency mixing orientation. Together, these form the final multi-objective decision-making solution set, providing theoretical foundations and data support for the design and operation of mixing equipment.

3. Results and Discussion

3.1. Analysis of CFD Simulation Results

To elucidate the influence mechanism of solid-phase volume fraction on the flow field, solid-phase distribution, and vortex structure in the stirred system, this section selects a typical operating condition with 20% solid-phase volume fraction within the optimal prediction range. A systematic analysis is conducted from three dimensions: macroscopic flow field characteristics, dynamic distribution patterns of the solid-phase, and radial/lateral distributions of local parameters.

3.1.1. Macroscopic Flow Field Characteristics

By combining the simulation streamline distribution diagram, the macroscopic flow characteristics of the fluid field inside the reactor can be visually observed. As shown in Figure 6, the stirring blades continuously rotate and drive the surrounding fluid, promoting the formation of a closed-loop axial circulation flow field within the reactor. From the streamline characteristics of the longitudinal section, the fluid exhibits an up-and-down churning flow pattern, with an overall gradient distribution of velocity. The velocity peaks in the region near the blade tips, while it significantly decreases near the reactor wall and bottom. This distribution pattern aligns with the flow field characteristics typical of industrial mixing of high-viscosity media. The flow field characteristics observed in the high-viscosity system of this study are consistent with the CFD simulation results reported by Tamburini et al. [6] in a dense solid–liquid suspension reactor. Specifically, high-speed jets at blade tips impact the wall and generate secondary vortices. Under high-viscosity conditions, these high-speed jets in the blade region serve as the primary driving force for overall circulation. The formation of secondary vortices enhances mass transfer in the wall vicinity. Furthermore, the multi-scale vortex-coupled flow field observed in this study qualitatively aligns with the "cooperative enhancement of main and secondary vortices during mixing" phenomenon identified by Qiu et al. [7] in a rigid-flexible paddle mixer, further validating the simulation results.

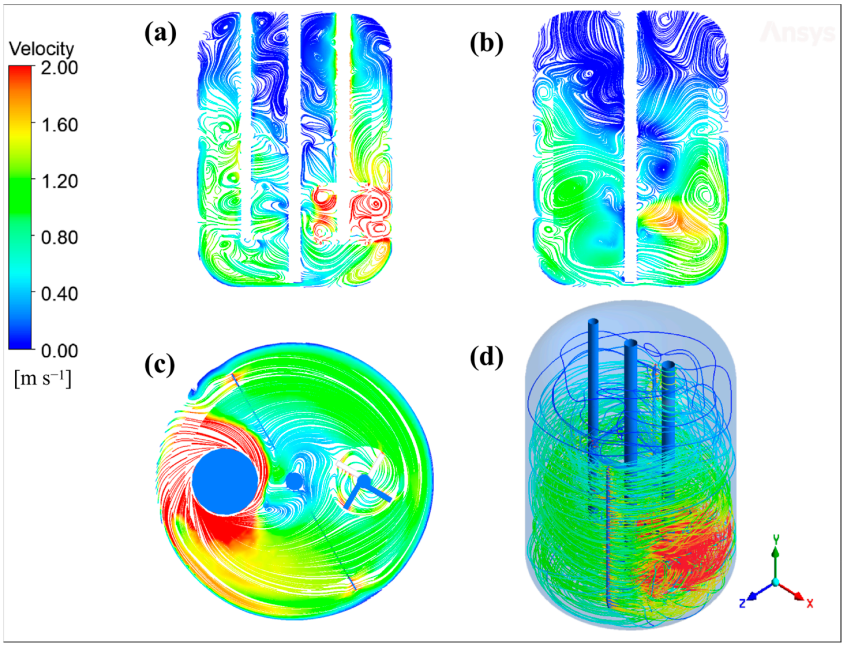


Figure 6. Streamline diagram displayed in velocity form. (**a**) xy-plane; (**b**) yz-plane; (**c**) xz-plane; (**d**) overall flow field.

Further in-depth analysis based on the top view and three-dimensional streamlines reveals that the high-speed jet flow from the blades impacts the reactor wall, generating secondary vortex structures. The primary and secondary vortices within the system collectively form a multi-scale coupled vortex field. From the perspective of mixing mechanisms, the high-velocity region near the blade tips can break up solid particle agglomerates through strong shear forces. Meanwhile, the multi-scale vortex structures distributed throughout the system drive radial and axial fluid migration, effectively mitigating particle sedimentation at the bottom. This flow mechanism is the core factor in achieving uniform suspension of solid particles, enhancing interphase mass transfer efficiency, and improving overall mixing quality.

Figure 7 reveals a significant stratified enrichment phenomenon of solid particles in this high-viscosity solid–liquid mixing system: the solid-phase volume fraction is notably higher at the bottom of the reactor, while the filler concentration in the top region is relatively insufficient, resulting in uneven material distribution vertically. The underlying mechanism lies in the high viscosity of polyurethane adhesive, which leads to poor fluid mobility and substantial resistance to axial particle migration. Additionally, under the combined effects of gravity and centrifugal force from agitation, high-density solid particles tend to settle and aggregate. This ultimately causes non-uniform distribution with material accumulation at the bottom and deficiency at the top. This is a common technical challenge in high-viscosity non-Newtonian biphasic mixing operations. Furthermore, the corresponding three-dimensional solid-phase volume fraction cloud map fully illustrates the spatial enrichment pattern of particles throughout the reactor, visually exposing defect areas such as local material accumulation and particle voids. This not only aids in analyzing the influence of solid-phase volume fraction on suspension characteristics but also provides intuitive and reliable visual data support for subsequent quantitative calculations of solid-phase uniformity and optimization of process parameters.

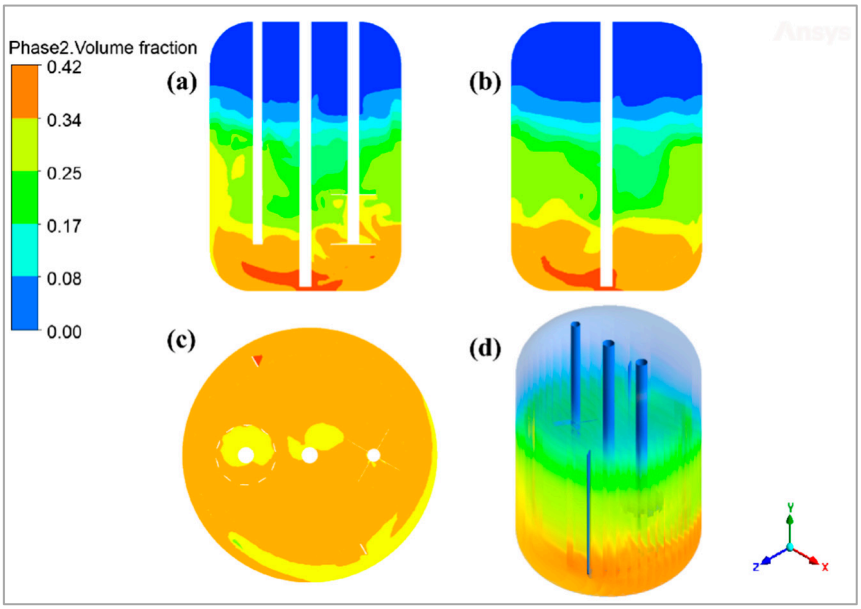


Figure 7. Volume distribution of the second solid phase. (**a**) xy-plane; (**b**) yz-plane; (**c**) xz-plane; (**d**) overall flow field.

By analyzing the vortex structure distribution cloud maps corresponding to different vorticity thresholds, Figure 8 clearly reveals the evolution law of the vortex field and its mechanism of action on mixing performance. The vorticity threshold can filter flow vortices of different intensities, directly determining the spatial coverage range of vortex structures.

When the threshold is set at vorticity = 0.04, high-intensity vortices only form in the tip region of the stirring paddle, acting on the local fluid with a very limited range. As the threshold is gradually reduced to 0.01, low-intensity secondary vortices are included in the statistical range, causing vortices to spread outward from localized areas and form a multi-level, multi-scale coupled vortex field that integrates both axial and radial directions. From the perspective of mixing mechanism analysis, a globalized vortex field can enhance the fluid replacement efficiency within the reactor, effectively solving the problem of solid particle sedimentation in high-viscosity systems, further optimizing particle dispersion effects, and significantly improving overall mixing quality.

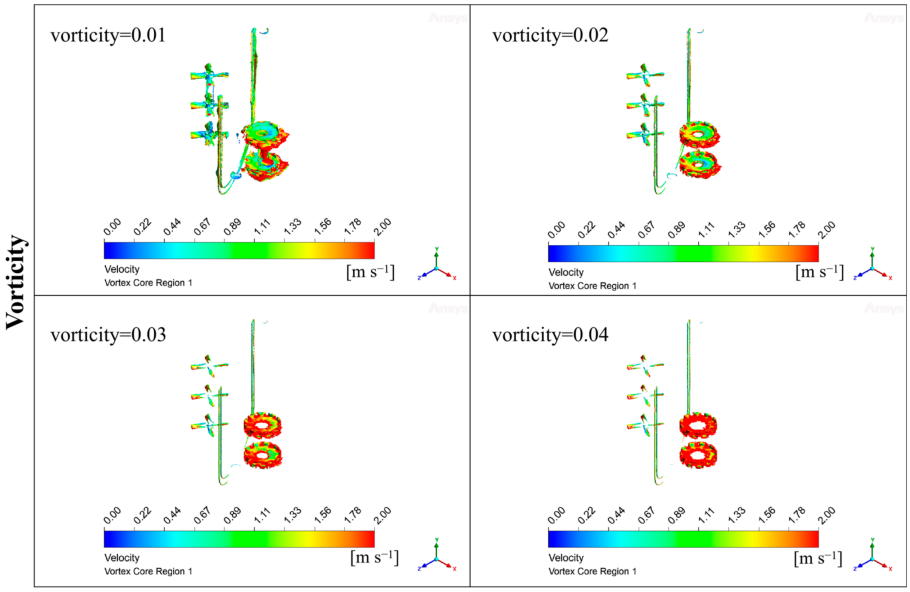


Figure 8. Vorticity distribution at different levels.

Furthermore, to comprehensively evaluate the impact of solid-phase volume fraction on mixing performance, this study selected three representative conditions with low, medium, and high solid-phase volume fractions (10%,20%, and 30%). Combining the Z-plane solid-phase volume fraction distribution cloud map (Figure 9) with quantitative parameters, we analyzed the relationship between solid-phase distribution and mixing performance.

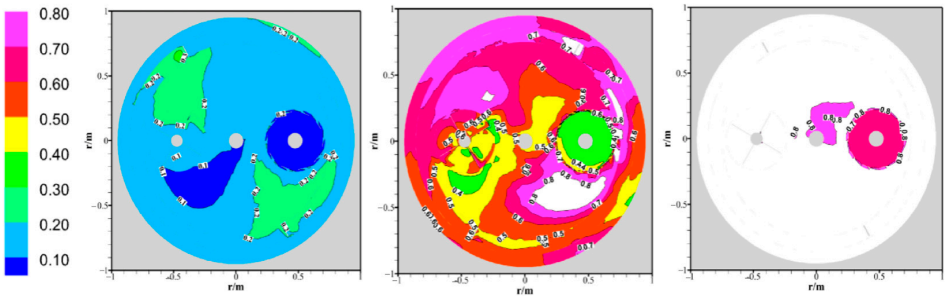


Figure 9. Solid-phase distribution results at 10 s for solid-phase volume fractions of 10%, 20%, and 30%.

As shown in Figure 9, at a solid-phase volume fraction of 10%, the distribution of solid particles is relatively sparse, primarily concentrated near the agitator with lower concentrations in other tank regions. At 20%, the distribution becomes more uniform with reduced concentration variations across areas, while concentrations near the agitator and in the central tank region significantly increase. At 30%, overall concentrations are

higher with a more concentrated distribution, reaching 0.7–0.8 near the agitator and at the tank bottom, though slight gradients remain in certain areas. Quantitative data indicate that agitation power increases with rising solid-phase volume fraction (1,109,009.18 W, 1,307,679.842 W, 1,528,224.413 W). This is consistent with the physical mechanism of increased system viscosity and flow resistance under high-solid conditions. Solid-phase uniformity improves with higher solid-phase volume fraction (0.318, 0.383, 0.431), suggesting enhanced suspension and dispersion of solid particles. The volume-average shear rate slightly decreases (3.250 s^{-1}, 3.148 s^{-1}, 2.996 s^{-1}), likely due to weakened shear effects caused by elevated fluid viscosity. Finally, mixing uniformity declines with increasing solid-phase volume fraction (0.694, 0.458, 0.328), reflecting greater mixing challenges under high-solid conditions.

3.1.2. Dynamic Evolution Law of Solid-Phase Volume Fraction

By analyzing the time-series cloud images of solid-phase volume fraction on the Z-plane, the diffusion and migration patterns of solid particles in high-viscosity systems over stirring duration can be fully revealed. Based on the material distribution characteristics, the mixing process can be divided into three typical stages. As shown in Figure 10, during the initial stirring phase (0~10 s), influenced by gravity, the majority of solid particles accumulate near the bottom of the vessel and around the stirring shaft, resulting in severe material aggregation and significant differences in solid-phase volume fraction within the vessel, leading to extremely poor overall mixing.

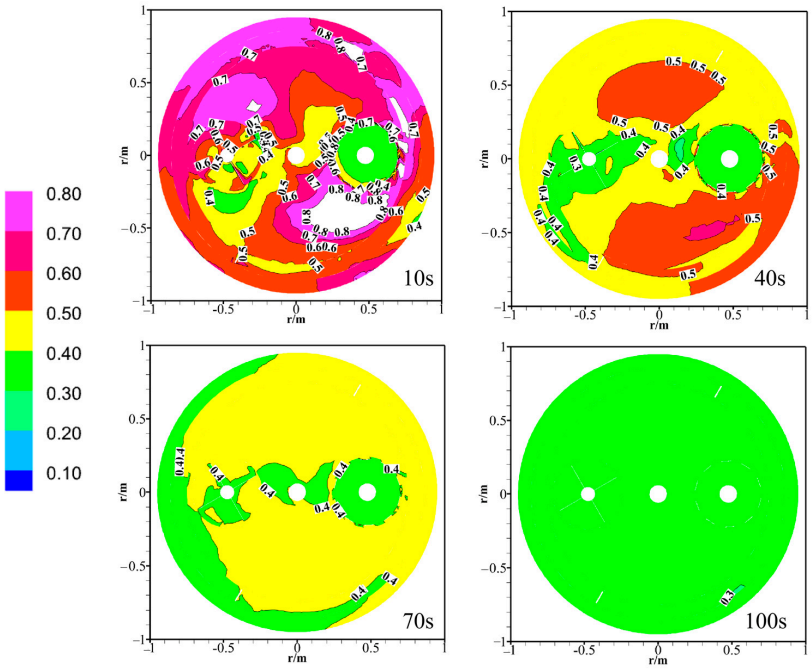


Figure 10. Distribution cloud map of solid-phase volume fraction on the Z-plane under different stirring durations.

Upon entering the rapid mixing phase (10~70 s), under the shear and entrainment effects of multiple stirring structures, localized high-concentration material clusters gradually break apart and disperse. Particles complete axial and radial migration across the entire domain via the circulating flow field, with the solid-phase volume fraction difference continuously decreasing.

In the later stirring phase (70~100 s), the particle distribution state remains largely unchanged, and the system progressively reaches dynamic equilibrium, entering the steady-state mixing stage. This phased evolution characteristic visually reflects the challenges of

mixing high-viscosity media and provides direct data support for setting stirring durations and optimizing mixing efficiency in such systems. In this study, the solid-phase particles exhibited an asymmetric layered distribution characterized by "enrichment at the bottom and depletion at the top," a phenomenon consistent with the particle sedimentation behavior observed by Kasat et al. [14] in solid–liquid stirred reactors. Kasat et al. demonstrated that in high-viscosity systems, the competition between gravitational settling and convective transport is the fundamental cause of uneven axial distribution. The quantitative results further indicate that after 180 s of mixing time, the solid-phase volume fractions at all monitoring points converged; this time scale falls within the same order of magnitude as the mixing time (150–200 s) reported by Shuai et al. [4] in high-viscosity non-Newtonian fluid twin-shear mixers, thereby indirectly validating the predicted mixing duration in this study.

By analyzing the time-varying curves of solid-phase volume fraction from multiple monitoring points, the dynamic diffusion and convergence patterns of solid particles in high-viscosity mixing systems can be quantitatively examined, supplementing the qualitative characteristics of the mixing stages discussed earlier. As shown in Figure 11, during the initial mixing phase, the solid-phase volume fraction values at different monitoring points vary significantly due to the combined effects of particle sedimentation characteristics and high-viscosity fluid resistance, with peak differences reaching 0.2, clearly reflecting the severe initial material distribution imbalance. As mixing continues, under the shear disturbance of multiple stirring structures and the transport effect of the circulating flow field, the high-concentration materials gradually diffuse. The solid-phase fraction curves at each monitoring point progressively converge with reduced fluctuation amplitudes. When the mixing duration reaches 180 s, the solid-phase volume fraction values at all monitoring points synchronize and stabilize around 0.28 without further fluctuations, indicating that the solid–liquid system in the reactor has overcome local segregation and entered a fully mixed steady state. This quantitative evolution pattern not only accurately defines the optimal mixing duration for this specific condition but also provides a quantitative basis for determining mixing time and setting stirring process parameters in similar high-viscosity polyurethane adhesive systems.

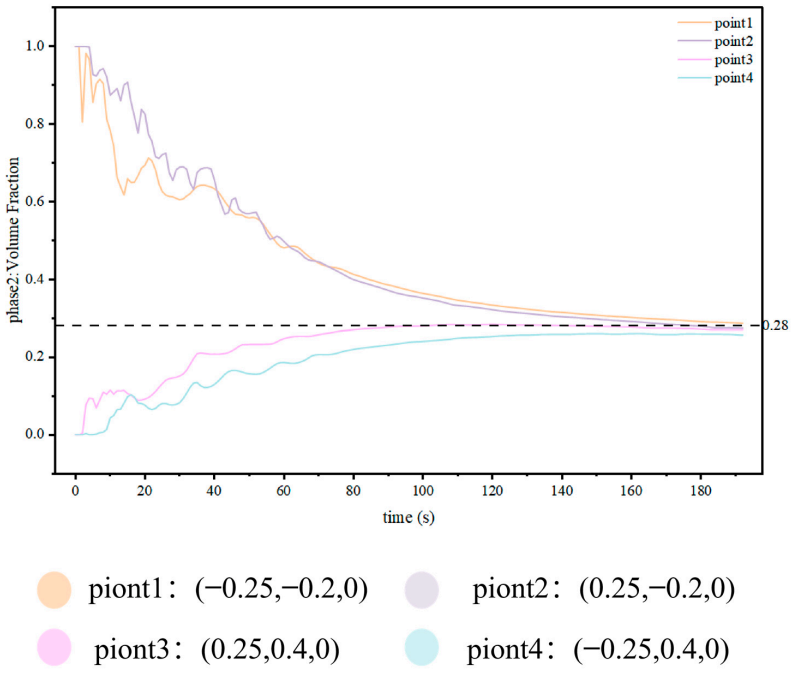


Figure 11. Variation curve of solid-phase volume fraction at multiple monitoring points.

3.1.3. Local Parameter Radial and Transverse Distribution Characteristics

By analyzing the radial and transverse cross-sectional parameter distribution curves, a comprehensive understanding of the spatial distribution characteristics of flow velocity and solid-phase volume fraction inside the stirred tank can be achieved, revealing the intrinsic patterns of particle migration across different dimensions. From the radial cross-section perspective (Figure 12), the fluid velocity decreases gradiently outward from the central axis, peaking at the core region and approaching zero near the tank wall due to wall resistance. Driven by centrifugal force, suspended solid particles gradually accumulate toward the wall side, resulting in a solid-phase distribution characterized by lower concentrations at the center and higher concentrations at the periphery, demonstrating a clear negative correlation.

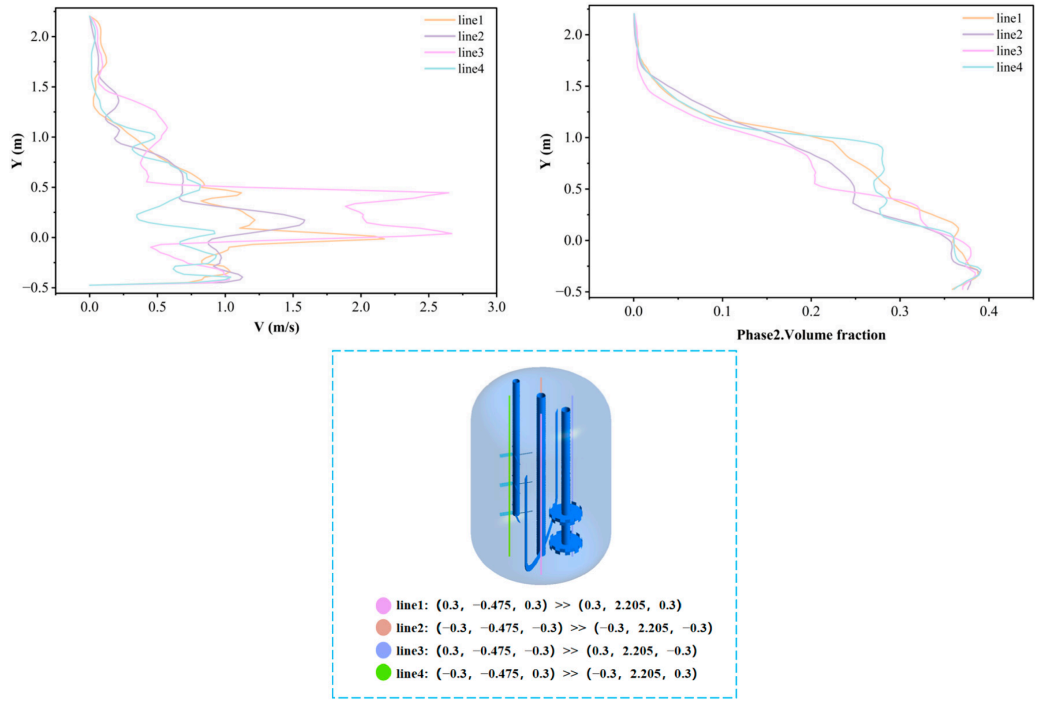


Figure 12. Distribution curves of radial velocity and solid-phase volume fraction.

From the transverse cross-section analysis (Figure 13), the velocity distribution exhibits an overall symmetrical pattern, with peak velocities precisely corresponding to the positions of the impeller groups. However, due to the coupled disturbances from the combined effects of the propeller, anchor, and dispersing structures, the solid-phase volume fraction does not form a symmetrical distribution, showing significant fluctuations in localized regions.

Integrating these two distribution patterns reveals that multidimensional flow field variations, centrifugal effects, and the complex impeller structure are the primary causes of uneven flow velocity and solid-phase segregation within the tank. This conclusion further explains the inherent challenges in mixing high-viscosity systems, where localized material accumulation is prone to occur.

3.2. Machine Learning Model Construction and Multi-Objective Optimization

3.2.1. Enhanced Dataset Construction Based on Cubic Spline Interpolation

To address the issue of insufficient original CFD samples and the tendency of models to underfit, this study adopts a standardized data processing workflow. This workflow involves preliminary dataset partitioning with exclusive training set augmentation. It also avoids data leakage and ensures the generalization performance of surrogate models. The research first randomly divides 12 sets of original CFD simulation samples, designating

8 sets as the foundational training set and the remaining 4 independent real-case scenarios (solid-phase volume fractions of 0.10, 0.12, 0.23, and 0.32) as the isolated test set. The test set remains entirely excluded from data augmentation, model training, and hyperparameter tuning throughout the process, serving solely for the final validation of model generalization capability. Building on this, an adaptive cubic spline interpolation algorithm is employed to expand only the foundational training set, with the newly generated virtual samples strictly adhering to fluid mixing physical laws. The original real samples and interpolated virtual samples are then integrated to form an augmented training set comprising 43 samples. This dataset encompasses five core performance parameters across varying solid-phase volume fractions. These parameters include stirring power, solid-phase uniformity, and shear rate. The dataset enriches sample gradients while effectively broadening the model's parameter adaptation range. The dataset structure is illustrated in Table 3.

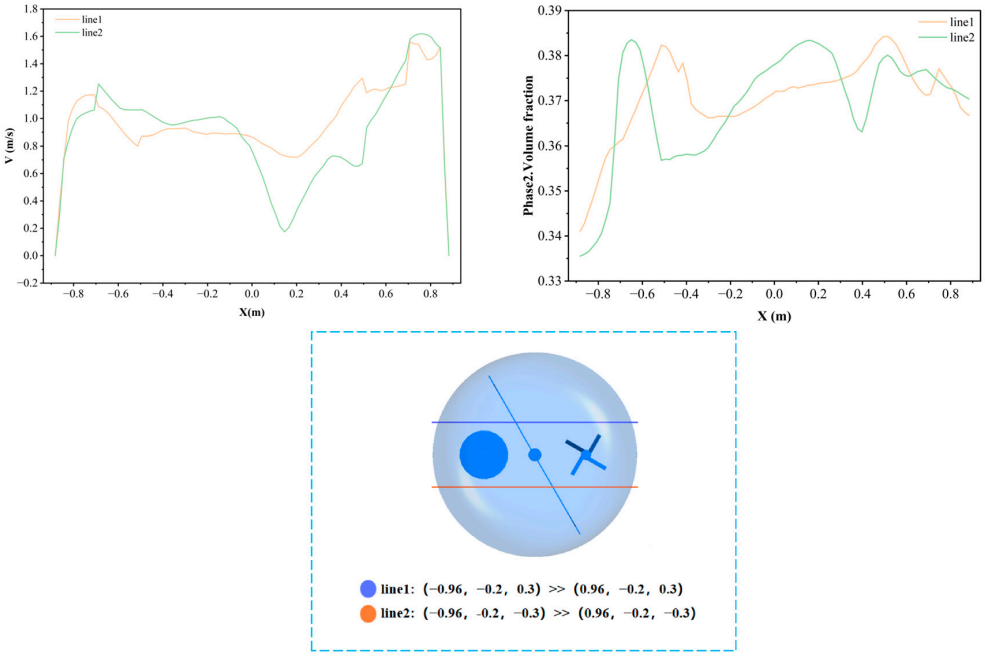


Figure 13. Distribution curves of horizontal velocity and solid-phase volume fraction.

Table 3. Example of the Enhanced Training Dataset (Partial).

Sample Type	Solid-Phase Volume Fraction Rate	Mixing Power (W)	Uniformity of Solid-Phase Distribution	Volume Average Shear Rate (s^{-1})	Mixing Time (s)	Final Mixing Uniformity
True value	0.08	1,052,946.337	0.30056	3.330556151	9.85	0.750551128
Virtual value	0.094	1,065,427.139	0.310825	3.3033921	9.82	0.713190091
Virtual value	0.094285	1,071,941.875	0.310556714	3.304848458	9.847142857	0.715012692
Virtual value	0.108	1,077,907.941	0.32109	3.276228049	9.79	0.675829054
…	…	…	…	…	…	…
True value	0.15	1,115,350.349	0.351885	3.194735895	9.7	0.563745942
Virtual value	0.151428	1,147,924.03	0.350543571	3.202017683	9.835714286	0.572858949
…	…	…	…	…	…	…

3.2.2. Agent Model Training and Quantitative Evaluation

Based on the augmented training dataset, this study simultaneously completed the training and debugging of two small-sample adaptation models, GPR and SVR. The comprehensive performance of the models was quantitatively evaluated using three metrics: RMSE, MAE, and R^2. The evaluation was conducted with an isolated test set. The results

are shown in Figure 14. The test results indicate a significant gap in predictive performance between the two models: the GPR model achieved an MAE of only 0.021741 and an RMSE of 0.027163, far lower than the SVR model's 0.41111 and 0.475569, demonstrating significantly smaller prediction deviations. Additionally, the GPR model's coefficient of determination (R^2) reached 0.968, explaining nearly 97% of the data's dispersion characteristics, indicating a near-ideal fit. In contrast, the SVR model's R^2 value was 0, failing to effectively capture the nonlinear relationship between process parameters and performance indicators, with its predictive accuracy equivalent to basic mean fitting. Considering all evaluation metrics, the GPR model is determined to be the optimal surrogate model for this study.

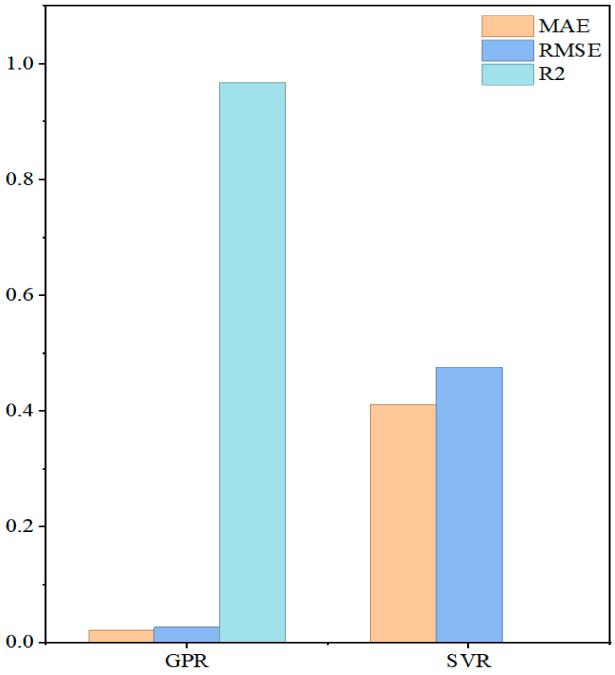


Figure 14. Comparison of evaluation metrics for two types of machine learning models.

The SVR model in this study adopted the RBF kernel function with hyperparameters set to C = 10, ε = 0.05, and γ = 2. The poor performance of the SVR model compared with the GPR model can be attributed to three factors. First, GPR is a probabilistic non-parametric Bayesian method. It can automatically learn data structure through kernel functions even with small samples. In contrast, SVR relies heavily on the number of support vectors, which is severely limited with only 36 training samples. Second, the input variable in this study is only one-dimensional (solid-phase volume fraction), which restricts the advantage of SVR's kernel method. Third, this study involves five output variables; SVR models each output independently without sharing cross-output information, while GPR's probabilistic framework utilizes limited data more effectively. This finding itself constitutes an important contribution of this study: for small-sample, low-dimensional-input, multi-output CFD-ML scenarios, GPR demonstrates superior applicability over SVR.

3.2.3. Comparative Analysis of Model Prediction Performance

By integrating the multi-dimensional prediction results shown in Figure 15, a comprehensive comparison of the fitting performance between the two models can be conducted. This comparison is based on five key operational indicators, including stirring power, volume-averaged shear rate, and solid-phase distribution uniformity, further validating the accuracy of the aforementioned evaluation metrics. Overall, the GPR model demonstrates highly consistent predictions with the CFD simulation results across all performance metrics, exhibiting superior comprehensive predictive capabilities compared to the SVR model.

In high-magnitude indicators such as stirring power consumption and shear rate, the GPR model shows smaller fluctuation errors and excellent numerical stability. For relative indicators with smaller magnitudes, such as solid-phase uniformity and mixing time, it also achieves higher fitting accuracy. The performance gap between the two models stems from their underlying algorithmic principles: GPR, based on a Bayesian probability framework, quantifies prediction uncertainty, making it more suitable for this study's small-sample, highly nonlinear viscous mixing system. In contrast, SVR's fixed hyperplane solution approach fails to accurately capture the coupling relationships between multi-scale flow fields and process parameters. Considering both error metrics and prediction fitting performance, this study ultimately selects GPR as the optimal surrogate model, providing data support for subsequent multi-objective intelligent optimization of solid-phase volume fraction.

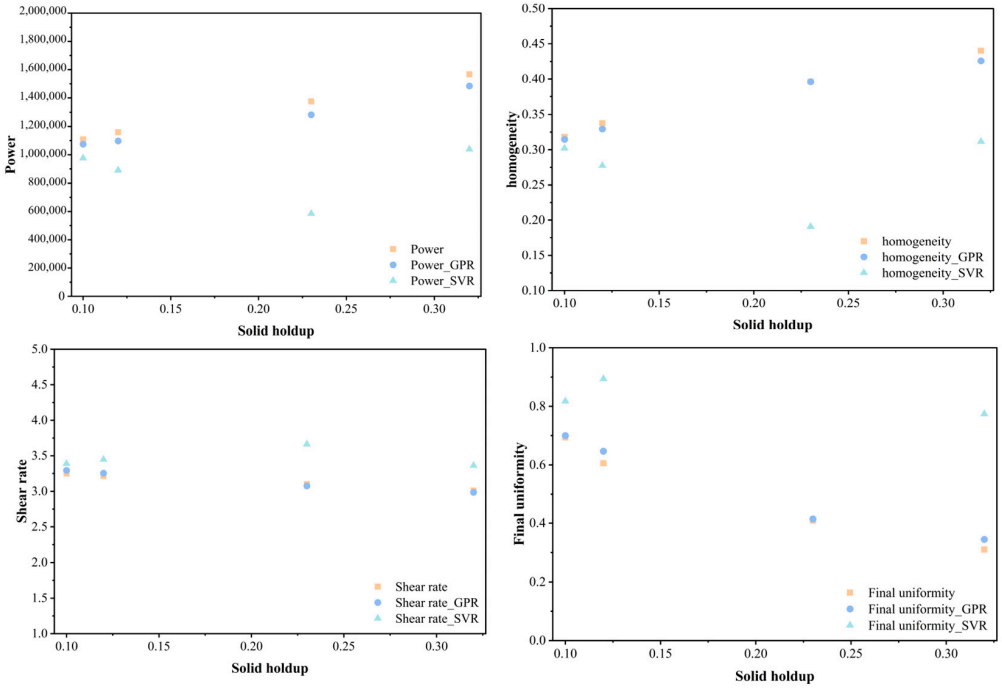


Figure 15. Comparison of GPR and SVR predictions.

3.2.4. Multi-Objective Optimization Analysis of Solid-Phase Volume Fraction

This section builds upon the pre-screened optimal GPR surrogate model, using the solid-phase volume fraction as the sole decision variable, and combines the NSGA-II algorithm to achieve five-dimensional multi-objective collaborative optimization. Figures 16 and 17 visually illustrate the response relationships between the solid-phase volume fraction (8~32%) and various mixing performance indicators, as well as the distribution of the Pareto non-dominated solution set.

From the objective function response curves in Figure 16, it can be observed that the solid-phase volume fraction exerts differentiated and mutually constraining effects on each evaluation metric. Clear quantitative trends are evident. As the solid-phase volume fraction increases, the mixing power consumption rises approximately linearly. It shows a significant increase when the solid-phase volume fraction grows from 8% to 32%. Meanwhile, the uniformity of solid-phase distribution improves steadily, and particle dispersion performance is effectively enhanced. However, excessively high solid-phase volume fraction exacerbates system viscosity, leading to a substantial decline in overall mixing uniformity.

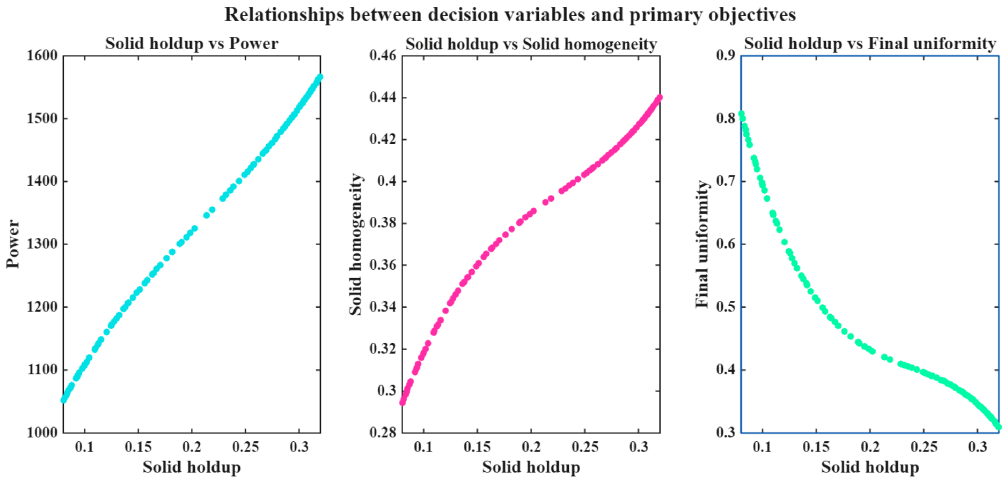


Figure 16. Relationship between solid-phase volume fraction and objective function response.

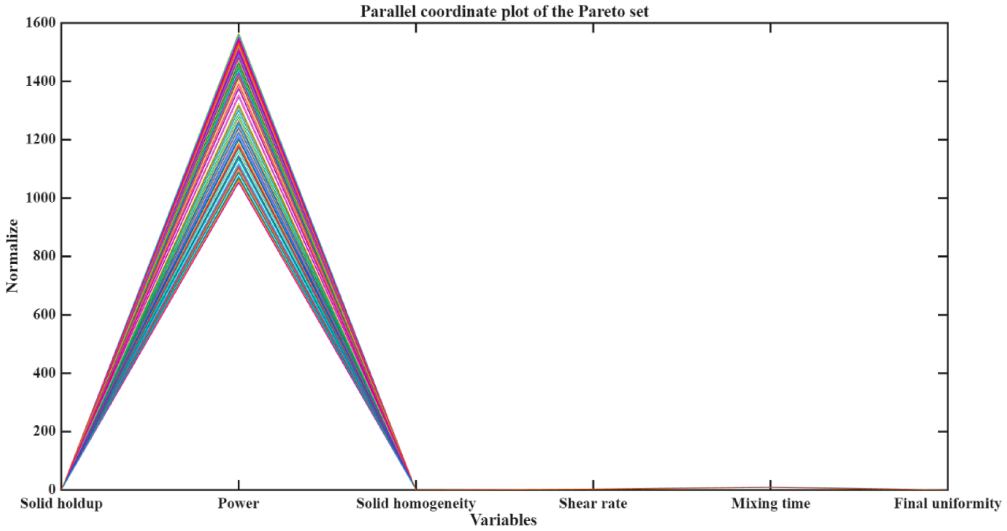


Figure 17. Parallel coordinate plot of the Pareto solution set.

By analyzing the parallel coordinate plot of the Pareto solution set in Figure 17, the optimization trade-offs can be further quantified. The core conflict in this multi-objective optimization lies between mixing power and solid-phase dispersion uniformity, which exhibit a strong positive-negative correlation and serve as the primary constraints for operational condition screening. In contrast, other evaluation metrics such as volume-averaged shear rate and mixing time show minimal fluctuations across the Pareto solution set, with low sensitivity and weak responses to changes in solid-phase volume fraction, indicating they are not dominant limiting factors in this optimization.

These quantitative patterns clearly elucidate the trade-off mechanisms among objectives. They provide theoretical support for subsequent practical production needs. These include balancing energy consumption, dispersion efficiency, and mixing quality. This helps identify the optimal solid-content conditions tailored to different production scenarios. The three optimal operating conditions identified in this study exhibit similar trade-off patterns compared to the multi-objective optimization results of radial stirred tanks obtained by Zhao et al. [16] using the CFD-ML method. These conditions are balanced mode at 15%, low-energy mode at 8%, and highly dispersed mode at 32%. Zhao et al. similarly found that reducing solid-phase volume fraction significantly lowers energy consumption but compromises dispersion uniformity, and vice versa, thereby confirming the universality of solid-phase volume fraction as a key trade-off variable.

Based on the Pareto non-inferior solution set and considering diverse production scenarios, this study uses the ideal point decision criterion to identify three representative optimal conditions. These conditions balance energy consumption and mixing performance, with detailed parameters listed in Table 4. The balanced condition, with a solid-phase volume fraction of approximately 15%, strikes a compromise between stirring power consumption and solid-phase dispersion, making it suitable for conventional large-scale production. The power-optimized condition sets the solid-phase volume fraction at 8%, minimizing stirring energy consumption at the cost of reduced particle dispersion performance, thus aligning with low-cost production models. The solid-phase uniformity-optimized condition adopts a high solid-phase volume fraction of 32%, enhancing particle suspension by increasing energy consumption to meet the requirements for high-quality adhesive production. These three conditions correspond to balanced production, energy-saving and cost reduction, and high-quality preparation, respectively, providing direct and quantifiable process guidance for adjusting solid-phase volume fraction parameters in 5000 L industrial mixing reactors.

Table 4. Recommended Operating Conditions.

Working Condition	Solid-Phase Volume Fraction Rate	Mixing Power (W)	Uniformity of Solid-Phase Distribution
Balanced (Optimal Overall)	0.14741108	1220.486807	0.358589577
Power optimization	0.08	1052.288125	0.294459492
Optimal solid-phase uniformity	0.32	1567.17495	0.440226

To facilitate practical factory implementation, concrete guidance is proposed. First, for measurement and control, operators should adopt gravimetric dosing (e.g., loss-in-weight feeders) to strictly control solid-phase volume fraction to target values (8%, ~15%, or 32%), while maintaining the impeller speed constant. Based on the data in Table 4, compared with the balanced mode (solid-phase volume fraction 14.74%, power 1220.49 W, uniformity 0.3586), the low-energy mode (solid-phase volume fraction 8%) reduces power by 13.78% but decreases uniformity by 17.88%. This represents a saving of 168.20 W. The high-dispersion mode (solid-phase volume fraction 32%) improves uniformity by 22.75% but increases power by 28.40%. These explicit trade-offs provide direct guidance for users to select the optimal operating mode based on their specific production priorities. Second, regarding sensitivity to fluctuations, the balanced condition (~15%) offers the highest robustness. Conversely, the 8% and 32% conditions are highly sensitive; slight positive deviations may cause equipment overload or yield-stress-induced flow deadlock, respectively. Finally, for online monitoring, real-time torque sensors and motor current feedback loops should be installed. Since torque is highly sensitive to viscosity changes, it can serve as a proxy for solid-phase volume fraction. If monitored values deviate from model predictions, the control system should adjust the feeding rate to prevent mixing failure.

4. Conclusions

This study focuses on a 5000 L industrial-scale high-viscosity polyurethane adhesive solid–liquid two-phase mixing system, coupling CFD numerical simulation with machine learning algorithms to systematically investigate the influence mechanism of solid-phase volume fraction on the mixing flow field, particle distribution, and comprehensive mixing

performance, while achieving multi-objective intelligent parameter optimization. The main findings are as follows:

(1) Based on simulation conditions spanning a wide range of 8~32%, a comprehensive solid–liquid mixing performance database was established, revealing the dual-impact mechanism of solid-phase volume fraction. Increasing the solid-phase volume fraction enhances the suspension and dispersion capability of solid particles but significantly raises system viscosity and mixing energy consumption, while simultaneously deteriorating overall mixing uniformity. These performance indicators are mutually constrained.

(2) Adaptive cubic spline interpolation was employed for small-sample data augmentation, and strict dataset partitioning was implemented to avoid data leakage. Through multi-indicator comparative analysis, the Gaussian Process Regression (GPR) model demonstrated significantly superior prediction accuracy and generalization capability over the Support Vector Regression (SVR) model, accurately capturing the nonlinear mapping relationship between solid-phase volume fraction and five mixing performance metrics. The GPR model can serve as an efficient surrogate to replace repetitive CFD simulations.

(3) Using the NSGA-II algorithm, a five-objective collaborative optimization was conducted. It identified three optimal solid-phase volume fraction conditions tailored for different industrial scenarios: balanced, energy-efficient, and high-quality. Specifically, the balanced mode corresponds to a solid-phase volume fraction of 14.74%, with a stirring power of 1220.49 W and a solid-phase distribution uniformity of 0.3586. The low-energy mode (solid-phase volume fraction 8%) reduces power by 13.78% (saving 168.20 W) compared with the balanced mode, but decreases uniformity by 17.88%. The high-dispersion mode (solid-phase volume fraction 32%) improves uniformity by 22.75% but increases power by 28.40%.

This study fully validates the feasibility and superiority of the integrated optimization strategy combining "CFD numerical simulation + machine learning surrogate modeling + intelligent algorithm optimization" in the field of high-viscosity multiphase mixing. It provides novel research insights and standardized technical solutions for the intelligent and energy-efficient regulation of polyurethane adhesive and similar non-Newtonian fluid mixing processes.

This study adopted a Newtonian fluid assumption, simplifying the rheological behavior of actual polyurethane adhesives. While justified for the methodological focus, this may underestimate power consumption and mixing time at high solid-phase volume fractions (>25%) where non-Newtonian effects become pronounced. Future work incorporating non-Newtonian models validated by experiments is needed to improve accuracy and applicability. Meanwhile, optimizing only solid-phase volume fraction under constant stirring speed limits generalizability. This simplification was intentional to isolate the core influence of solid-phase volume fraction—the most critical parameter—and the three recommended modes provide actionable guidance. To enhance generalizability, future work should extend the decision space to include stirring speed and geometric parameters. Our modular CFD-ML architecture can seamlessly support multi-variable extensions, enabling co-optimization of process parameters and equipment geometry via NSGA-II, paving the way for comprehensive intelligent optimization. Additionally, this study is limited by a small CFD sample size (12 original cases). While the strict data isolation protocol mitigates overfitting risks, the 4-point test set is statistically slender. Future work will employ Leave-One-Out Cross-Validation (LOOCV) and larger-scale datasets to provide a more statistically robust assessment. Furthermore, due to the large scale of the 5000 L industrial reactor involved in this study, conducting full-scale experimental validation is challenging

at the current stage. Nevertheless, future work will consider scaled-down or pilot-scale experimental mixing tests to verify the CFD predictions and optimization outcomes, thereby enhancing the practical engineering reliability of the proposed framework.

Author Contributions: Conceptualization, B.H. and R.L.; methodology, B.H., X.T. and R.L.; software, L.F.; validation, L.F. and X.T.; formal analysis, L.F.; investigation, L.F. and R.L.; resources, B.H. and X.T.; data curation, B.H., L.F. and X.T.; writing—original draft preparation, B.H. and L.F.; writing—review and editing, B.H., X.T. and R.L.; visualization, B.H.; supervision, B.H. and R.L.; project administration, B.H., X.T. and R.L.; funding acquisition, B.H., X.T. and R.L. All authors have read and agreed to the published version of the manuscript.

Funding: This research was funded by projects for technological innovation and application development in Chongqing (CSTB2023TIAD-KPX0018) and Shanghai Hansi Industrial Co. (grant number H20250293).

Data Availability Statement: Data will be made available on request.

Acknowledgments: During the preparation of this hypothetical paper, DeepSeek-V4 was used solely for language editing and formatting. All core hypotheses, theoretical frameworks, data analysis, and scientific conclusions were independently developed and verified by the authors.

Conflicts of Interest: The authors declare that they have no known competing financial interests or personal relationships that could have appeared to influence the work reported in this study. The authors declare that this study received funding from Shanghai Hansi Industrial Co. The funder was not involved in the study design, collection, analysis, interpretation of data, the writing of this article, or the decision to submit it for publication.

References

1. Wu, H.; Wen, T.; Ding, Q.; Zhang, J.; Du, G.; Charrier, B.; Essawy, H.; Pizzi, A.; Yuan, Z.; Zhou, X.; et al. A sustainable adhesive via one-pot simple preparation derived from bio-sourced phytic acid and corn starch for green wood panels: Ideal bonding performance and ultra-high flame retardancy. *Chem. Eng. J.* **2025**, *508*, 161026. [CrossRef]
2. Cai, K.; Zuo, S.; Luo, S.P.; Yao, C.; Liu, W.; Ma, J.; Mao, H.; Li, Z. Preparation of polyaniline/graphene composites with excellent anti-corrosion properties and their application in waterborne polyurethane anticorrosive coatings. *RSC Adv.* **2016**, *6*, 95965–95972. [CrossRef]
3. Balbinot, G.d.S.; Leitune, V.C.B.; Montenegro, S.D.; Collares, F.M. Silver core-shells particles as antibacterial filler for adhesive resins. *Int. J. Adhes. Adhes.* **2025**, *138*, 103916. [CrossRef]
4. Galindo-Rosales, F.J.; Rubio-Hernàndez, F.J. Static and dynamic yield stresses of aerosil (r) 200 suspensions in polypropylene glycol. *Appl. Rheol.* **2010**, *20*, 22787.
5. He, B.; Fan, L.; Teng, X.; Qiu, F.; Liu, R. CFD-simulation-based multi-axial differential mixing enhancement study for high-viscosity adhesives: From the perspective of breaking the symmetry of the flow field. *Symmetry* **2025**, *17*, 1932. [CrossRef]
6. Tamburini, A.; Cipollina, A.; Micale, G.; Brucato, A.; Ciofalo, M. CFD simulations of dense solid–liquid suspensions in baffled stirred tanks: Prediction of suspension curves. *Chem. Eng. J.* **2011**, *178*, 324–341. [CrossRef]
7. Qiu, F.; Liu, Z.; Liu, R.; Quan, X.; Tao, C.; Wang, Y. Gas-liquid mixing performance, power consumption, and local void fraction distribution in stirred tank reactors with a rigid-flexile impeller. *Exp. Therm. Fluid Sci.* **2018**, *97*, 351–363. [CrossRef]
8. Shuai, Y.; An, S.; Hong, X.; Huang, Z.; Liao, Z.; Wang, J.; Yang, Y. Numerical simulation of hydrodynamics and mixing characteristics of high-viscosity non-Newtonian fluid in twin-shaft kneaders. *Ind. Eng. Chem. Res.* **2024**, *63*, 5931–5941. [CrossRef]
9. Zheng, C.; Zhang, M.; Qiu, S.; Li, H.; Wang, T.; Wang, H. Numerical simulation and experimental investigation of gas-liquid two-phase flow in a complex microchannel. *Chem. Eng. Sci.* **2021**, *230*, 116198. [CrossRef]
10. Li, A.; Yao, Y.; Zhang, X.; Wan, Y.; Li, P.; Wang, Y.; Tao, C.; Liu, Z. Using CFD and machine learning to explore chaotic mixing in laminar diameter-transformed stirred tanks. *Chem. Eng. J.* **2024**, *499*, 156201. [CrossRef]
11. Hu, L.; Pan, C.; Hu, D.; Yan, H.; Qiu, F.; Cheng, Z. Coupled CFD-machine learning optimization of inlet water-jet orifices in jet impact negative pressure reactors. *J. Taiwan Inst. Chem. Eng.* **2025**, *175*, 106248. [CrossRef]
12. Trávníková, V.; Von Lieres, E.; Behr, M. Quantifying Data Needs in Surrogate Modeling for Flow Fields in Two-Dimensional Stirred Tanks with Physics-Informed Neural Networks. *Phys. Fluids* **2025**, *37*, 117112. [CrossRef]

13. de Oliveira Maionchi, D.; Coimbra, N.D.; da Silva, J.G.; Santos, F.P.D. Predictive Model and Optimization of Micromixers Geometry Using Gaussian Process with Uncertainty Quantification and Genetic Algorithm. *Fluid Dyn. Res.* **2024**, *56*, 065504. [CrossRef]
14. Kasat, G.R.; Khopkar, A.R.; Ranade, V.V.; Pandit, A.B. CFD simulation of liquid-phase mixing in solid–liquid stirred reactor. *Chem. Eng. Sci.* **2008**, *63*, 3877–3885. [CrossRef]
15. Xu, P.; Liao, X.; Qiu, F.; Cheng, Z.; Li, W.; Liu, Z. Intelligent prediction of gas-liquid two-phase flow fields in jet impact negative pressure reactors: An integrated DA-WOA-CNN framework based on CFD. *Chem. Eng. Sci.* **2026**, *325*, 123495. [CrossRef]
16. Zhao, X.; Fan, H.; Lin, G.; Fang, Z.; Yang, W.; Li, M.; Wang, J.; Lu, X.; Li, B.; Wu, K.; et al. Multi-objective optimization of radially stirred tank based on CFD and machine learning. *AIChE J.* **2024**, *70*, e18324.
17. Jia, Z.; Zhang, S.; Fang, K.; Kong, B.; Xie, M.; Zhang, Q.; Yang, C. Assessment of stress-blended eddy simulation on prediction of flow characteristics in a Rushton impeller stirred tank. *Chem. Eng. Sci.* **2024**, *284*, 119442. [CrossRef]
18. Yang, G.; Yan, H.; Dong, Y.; Hu, L.; Hu, D.; Qiu, F. Multi-objective optimization of jet impact-negative pressure reactor based on computational fluid dynamics and machine learning. *Chem. Eng. Res. Des.* **2025**, *220*, 335–349. [CrossRef]
19. Pan, C.; Hu, L.; Qiu, F.; Cheng, Z.; Li, Z.; Guo, L. Theory and construction of machine learning-driven CFD agent model: A Bayesian-optimized CNN-LSTM framework. *J. Taiwan Inst. Chem. Eng.* **2026**, *182*, 106577. [CrossRef]
20. Thakur, H.; Verma, N.K.; Dhar, A.; Powar, S. Investigation of continuous stirred tank reactors for improving the mixing in anaerobic digestion: A numerical study. *Results Eng.* **2023**, *19*, 101317. [CrossRef]
21. Papadakis, L.; Schiel, M.; Vassilou, V.; Loizou, A.; Dilger, K. Adhesive bonding of attachments on alternate car shell surfaces in automotive final assembly lines. *Procedia CIRP* **2014**, *18*, 180–185. [CrossRef]
22. Qi, J.; Luo, T.; Yu, J.; Wang, C.; Chu, F.; Wang, J. Controllable structure, super adhesion, multifunctional, conductive pressuresensitive adhesive for electronic skin: Enhancing cohesion by cellulose-derived covalent crosslinking. *Chem. Eng. J.* **2024**, *499*, 156561. [CrossRef]
23. Zalc, J.M.; Alvarez, M.M.; Muzzio, F.J.; Arik, B.E. Extensive Validation of Computed Laminar Flow in A Stirred Tank with Three Rushton Turbines. *AIChE J.* **2001**, *47*, 2144–2154. [CrossRef]
24. Mao, C.; Hou, Y.; Wang, Y. Research on the Effects of Slurry Uniformity and Mixing Power of Continuous Cementing Slurry Mixers Based on Statistical and CFD Methods. *Geoenergy Sci. Eng.* **2023**, *233*, 212574. [CrossRef]
25. Gu, D.; Song, Y.; Xu, H.; Wen, L.; Ye, M. CFD Simulation and Experimental Analysis of Solid-Liquid Mixing Characteristics in a Stirred Tank with a Self-Similarity Impeller. *J. Taiwan Inst. Chem. Eng.* **2023**, *146*, 104878. [CrossRef]
26. Yuan, J.; Wang, Y.; Han, Z.; Qi, Y.; Yan, B.; Fan, Y.; Zhou, M.; Wang, Q. High-conversion-efficiency mode converters based on cubic spline interpolation. *Appl. Opt.* **2025**, *64*, 2269–2275. [CrossRef] [PubMed]
27. Jiang, X.; Chen, H.; Hui, H.; Zhang, K. A wind speed forecasting method using Gaussian process regression model under data uncertainty. *J. Fluids Eng.* **2025**, *147*, 031106. [CrossRef]
28. Kim, D.; Kim, D.; Ko, T.; Lee, S. Physics-informed Gaussian process regression model for predicting the fatigue life of welded joints. *Int. J. Fatigue* **2025**, *190*, 108644. [CrossRef]
29. He, N.; Liu, N.; Qian, C.; Li, R.; Liu, N.; Cheng, F.; Deng, Y. Air conditioning system load prediction using multi-kernel Gaussian process regression model with noisy observations built upon permutation entropy and fast Fourier transform. *Energy Build.* **2026**, *353*, 116906. [CrossRef]
30. Qu, S.; Guo, Y.; Leone, R.; Huang, M.; Li, P. An efficient sparse twin parametric insensitive support vector regression model. *Mathematics* **2025**, *13*, 2206. [CrossRef]
31. Cheng, K.; Li, D.; Deng, M.; Li, X.; Fang, G. Application of improved NSGA-II multi-objective genetic algorithm in optimal allocation of water resources in main tarim river basin. *Sustainability* **2025**, *17*, 1526. [CrossRef]
32. Kong, F.; Liu, Z.; Lin, C.; Wang, Z.; Wang, W.; Yao, S.; Zhang, W.; Zhang, J. Experimental study and parameter optimization of desiccant wheel-assisted atmospheric water harvesting system based on NSGA-II. *Energy Convers. Manag.* **2025**, *339*, 119943. [CrossRef]

Disclaimer/Publisher's Note: The statements, opinions and data contained in all publications are solely those of the individual author(s) and contributor(s) and not of MDPI and/or the editor(s). MDPI and/or the editor(s) disclaim responsibility for any injury to people or property resulting from any ideas, methods, instructions or products referred to in the content.